Geoderma 298 (2017) 35–45

Contents lists available at ScienceDirect

Geoderma

journal homepage: www.elsevier.com/locate/geoderma

Nickel speciation in several serpentine (ultramafic) topsoils via bulk synchrotron-based techniques

Matthew G. Siebecker [a,*], Rufus L. Chaney [b], Donald L. Sparks [a,c]

[a] University of Delaware, Delaware Environmental Institute (DENIN), Newark, DE 19716, USA
[b] United States Department of Agriculture, Adaptive Cropping Systems Laboratory, Beltsville, MD 20705, USA
[c] University of Delaware, Department of Plant and Soil Sciences, Newark, DE 19716, USA

ARTICLE INFO

Article history:
Received 28 April 2016
Received in revised form 23 February 2017
Accepted 10 March 2017
Available online xxxx

Keywords:
Nickel
Serpentine
Speciation
Ultramafic
Sonication
EXAFS
F-test
Hamilton test

ABSTRACT

Serpentine soils have elevated concentrations of trace metals including nickel, cobalt, and chromium compared to non-serpentine soils. Identifying the nickel bearing minerals allows for prediction of potential mobility of nickel. Synchrotron-based techniques can identify the solid-phase chemical forms of nickel with minimal sample treatment. Element concentrations are known to vary among soil particle sizes in serpentine soils. Sonication is a useful method to physically disperse sand, silt and clay particles in soils. Synchrotron-based techniques and sonication were employed to identify nickel species in discrete particle size fractions in several serpentine (ultramafic) topsoils to better understand solid-phase nickel geochemistry. Nickel commonly resided in primary serpentine parent material such as layered-phyllosilicate and chain-inosilicate minerals and was associated with iron oxides. In the clay fractions, nickel was associated with iron oxides and primary serpentine minerals, such as lizardite. Linear combination fitting (LCF) was used to characterize nickel species. Total metal concentration did not correlate with nickel speciation and is not an indicator of the major nickel species in the soil. Differences in soil texture were related to different nickel speciation for several particle size fractionated samples. A discussion on LCF illustrates the importance of choosing standards based not only on statistical methods such as Target Transformation but also on sample mineralogy and particle size. Results from the F-test (Hamilton test), which is an underutilized tool in the literature for LCF in soils, highlight its usefulness to determine the appropriate number of standards to for LCF. EXAFS shell fitting illustrates that destructive interference commonly found for light and heavy elements in layered double hydroxides and in phyllosilicates also can occur in inosilicate minerals, causing similar structural features and leading to false positive results in LCF.

1. Introduction

Serpentine soils have elevated amounts of trace metals, such as nickel, cobalt, and chromium versus non-serpentine soils. Identifying the nickel bearing minerals during soil weathering will allow for prediction of the potential mobility of nickel over the long term. These minerals strongly affect nickel solubility and mobility (Echevarria et al., 2006; Massoura et al., 2006).

Traditionally, sequential chemical extractions with increasingly aggressive reagents were used to identify soil metal species. Sequential extractions were effective in determining that nickel can accumulate partly in magnesium silicates and also with manganese and iron oxides (Cheng et al., 2011). However, sequential extractions are limited by the possibility of sample alteration, and it is difficult to compare studies on nickel solubility because often different sequential extraction procedures are used (Antic-Mladenovic et al., 2011). X-ray Absorption Spectroscopy (XAS) is capable of determining in situ metal speciation with minimal chemical sample treatment and was used in this study.

Because nickel is geogenic in serpentine soils and not anthropogenic (i.e., it is not from deposited aerosols emitted by smelters), apart from being sorbed to clay mineral surfaces and organic matter, nickel is commonly incorporated into the crystal lattices of clay, silt and sand-sized particles of the parent material and secondary minerals (Alexander et al., 2007a). Minerals common in serpentine soils, serpentinized peridotites, and ultramafic lateritic deposits that associate with nickel include those such as lizardite, antigorite, smectite, vermiculite, goethite and hematite (Cheng et al., 2011; Colin et al., 1990; Echevarria et al., 2006; Gaudin et al., 2005; Hotz, 1964; Massoura et al., 2006). Other studies have also shown nickel incorporation in silicate minerals (Decarreau et al., 1987; Hseu, 2006; Manceau and Calas, 1985). For XAS data, this means that nickel fluorescence emits from nickel sorbed to clay surfaces (e.g., iron and manganese oxides) and also from bulk

---

* Corresponding author.
E-mail addresses: mgs@udel.edu (M.G. Siebecker), Rufus.Chaney@ars.usda.gov (R.L. Chaney), dlsparks@udel.edu (D.L. Sparks).

http://dx.doi.org/10.1016/j.geoderma.2017.03.008
0016-7061/

parent material and larger-sized minerals still present in the whole soil fraction (e.g., lizardite). In order to discern between sorbed nickel phases and nickel incorporated into larger mineral phases, a sonication method was developed to remove clay coatings from the silt and sand fractions of the soils.

Several serpentine topsoils from Oregon, California and Maryland, USA were analyzed with the objective of characterizing the nickel species that naturally occur. Nickel species were identified in the sand, silt, and clay fractions using physical separation methods, sonication, bulk X-ray Diffraction (XRD), chemical digestion, and synchrotron radiation methods [e.g., Extended X-ray Absorption Fine Structure (EXAFS) spectroscopy]. Problems with the Linear Combination Fitting (LCF), a technique commonly used for EXAFS data analysis of soils, are presented and solutions are suggested by utilizing the F-test [Hamilton test, (Hamilton, 1965)] and employing shell fitting of Fourier-transformed EXAFS data. LCF of EXAFS data is commonly problematic in soils because of similar standards that can be used to fit the sample data. Substitution of similar standards and increasing or decreasing the number of standards by just one can have large impacts on the calculated percentage of each component. An averaged-based approach to determining percentage of components found from LCF is presented, which buffers LCF results from these large impacts.

2. Materials and methods

2.1. Physicochemical and mineralogical analysis

Soil samples from three sites were obtained for this study. The first and largest set of samples is from the Klamath Mountains, specifically the Cave Junction area of Josephine County in Southwest Oregon. The second set of samples is from the Jasper Ridge Biological Preserve in San Mateo County, CA and has been previously characterized (Oze et al., 2004). The third is a serpentine soil from Soldiers Delight Natural Environment Area near Baltimore, Maryland. The soils from Cave Junction and Soldiers Delight were sampled from field sites used for testing of nickel agromining and phytoremediation. They are all from the Ap horizon (0–15 cm). Initially they were partially dried and sieved to 4 mm. Then they were air dried and sieved to 2 mm. Further particle size fractionation is discussed in Section 2.2.

Soil elemental compositions were determined by a combination of digestion procedures including: microwave digestion with nitric acid (EPA method 3051), EPA method 3050B hot nitric, and an Aqua Regia method, all followed by ICP-OES. Particle size analysis was carried out by the hydrometer method. Citrate-dithionite extractions of the soils and soil fractions were also carried out to remove iron and manganese oxides and to determine nickel concentrations in the iron and manganese oxide fraction of the clay (Holmgren, 1967; Loeppert and Inskeep, 1996). Soil pH was determined by mixing the soil with distilled water in a 1:1 ratio and measuring the pH. Organic matter was determined by the loss-on-ignition (LOI) method. Elemental concentrations of the serpentine mineral standards were determined by complete dissolution of the mineral by a Katanax® Fusion machine with a mix of lithium tetraborate, metaborate, and bromide.

X-ray diffraction (XRD) was carried out on a Philips/Norelco powder diffraction system using Bragg-Brentano parafocusing optics with a graphite monochromator. Copper k-alpha radiation (8.04 keV) was used, operating at 35 kV and 20 mA. XRD was carried out on serpentine mineral standards obtained from the University of Delaware's mineralogical supply (serpentine mineral sample numbers 96, 185, and 5811). XRD was also carried out on the coarse sand, silt, clay and citrate-dithionite treated clay fractions of samples from Oregon and Maryland. Samples were powdered in mortar and pestle prior to XRD analysis. Additional XRD was carried out on synthetic nickel standards prepared in the laboratory and of bedrock (br) from the California soils (JR3br and COIIbr). Synthetic, nickel-doped mineral standards [magnetite, hematite, goethite, and ferrihydrite, and Ni-Fe layered double hydroxide (LDH) (2:1)] were made in the laboratory and characterized by XRD, EXAFS, and chemical digestion. Preparation methods of synthetic standards can be found in the Supplementary Materials. Mineral identification of diffraction data from the soils and soil fractions was carried out using Match!® software (Crystal-Impact, 2012).

2.2. Particle size fractionation via sonication method

Particle size fractionation was used to separate the whole soil fraction, to allow for identification of discrete nickel species located in the sand, silt, and clay size fractions. Other studies have shown nickel concentrations increase in the clay fraction (Oze et al., 2004) where particle sizes range from two micrometers to the nano-scale. This method, modified from published methods, served to disperse the clay fraction and separate the minerals by particle size and was designed to minimize the breakdown of particulate organic matter (i.e., sand-size OM) into smaller particles (Amelung and Zech, 1999; Amelung et al., 1998; Doelsch et al., 2006; Gimbert et al., 2005; Kahle et al., 2003; North, 1976; Oorts et al., 2005; Raine and So, 1994; Schmidt et al., 1999; Sohi et al., 2001; Solomon et al., 2002; Yang et al., 2009).

A probe tip sonicator was calibrated (North, 1976) using a 250 mL glass beaker. A slurry of 20 g of soil (<2 mm fraction) in 80 mL of 18.2 megohm water (1:4 soil:water ratio) was placed in the beaker for sonication. The probe was always placed 20 mm below the surface of the slurry. A Branson DIGITAL Sonifier® UNITS Model S-450D was used with a flat tip on the horn. Initially, 60 J/mL were applied to the slurry. Then the slurry was wet-sieved with a 250 μm sieve and 70 mL of water from a fine-mist, hand-pump spray bottle to yield a "sub-250 μm fraction". By using 70 mL the effluent was clear after passing through the 250 μm sieve. Then 440 J/mL were applied to the 150 mL of sub-250 μm fraction (Amelung et al., 1998). After the second sonication, the collected slurry was wet-sieved again using the spray bottle and a 45 μm sieve until the effluent was clear, yielding a "sub-45 μm fraction".

From the sub-45 μm fraction, first the <2 μm clay fraction and then the <5 μm clay/fine silt fraction were sequentially removed via centrifugation using a swinging-bucket centrifuge rotor. Then the 5–25 μm fraction (fine silt) was separated from the remaining sub-45 μm fraction via wet-sieving using a 25 μm sieve and the spray bottle until the effluent was clear, thus yielding a 25–45 μm fraction. The wet-sieved and centrifuged fractions were dried with warm air at 35 °C in typically <36 h. During every sonication the slurry was placed in an ice bath to maintain a slurry temperature of <37 °C. Particle density was assumed to be 2.65 g cm^{-1}.

For the rotor, the sedimentation distances were measured to calculate centrifuge time and speed. Centrifuge speed and time were calculated using a Sorvall RC 6 centrifuge with a HS-4 rotor, taking into account the R1 and R2 distances from the axis of rotation for sedimentation time and speed. Fifty mL conical centrifuge tubes were used. Centrifugation times were calculated from formulas in Soil Chemical Analysis Advanced Course (Jackson, 1985) pages 113 and 127 and Methods of Soil Analysis Part 4, Physical Methods (Gee and Or, 2002).

With respect to the rest of this paper, "clay" always refers to the <2 μm fraction; "silt" is the 25–45 μm silt fraction, and "coarse sand" or "coarse" or "sand" always refer to 0.5 to 1 mm diameter particles. Sonication disperses conglomerated clays and clays adsorbed to larger particles and minerals in the silt and sand fractions. These clays were washed out of the silt and sand fractions using the wet-sieving steps. Published methodologies using sonication for clay fraction separation generally do not provide laboratory-specific details; hence, the sonication times, centrifuge times, and decantation distances were all calculated using materials and equipment available for this study.

2.3. Synchrotron-based data acquisition and analysis

Additional methods for synchrotron-based data acquisition and analysis, including beamline characteristics, Principal Component

Analysis (PCA), Target Transformation (TT), SPOIL values, LCF, F-Test, and shell fitting methods of EXAFS data are described in the Supplementary Material text and Table S1. Linear Combination Fitting results were grouped into four different categories: "Mafic and Serpentine Related", "Iron Oxide", "Manganese Oxide", and "Adsorbed to phyllosilicate" (Table 3). The results were grouped in this fashion so all of the LCF results could be concisely categorized. The group "Mafic and Serpentine Related" includes multiple standards that, although distinct in origin and formation, are related in the local atomic environment of nickel. The standards that fall into this category are serpentine minerals (layered silicates), chain silicates, and layered hydroxides. Each standard is explicitly identified in Table S3. Nickel adsorbed to gibbsite (Yamaguchi et al., 2002) is included this group because it is similar to nickel incorporated into the octahedral layer of a light-element (aluminum) layered hydroxide mineral, which is similar to the hydroxide sheet in serpentine minerals (e.g., lizardite). The groups "Iron Oxide" and "Manganese Oxide" are standards where nickel is either adsorbed to the surface or incorporated (doped) into the structure of the iron or manganese oxides. Lastly, the category "Adsorbed to Phyllosilicate" is nickel adsorbed to montmorillonite clay at pH 6.

Linear combination fitting is sensitive to specific standards used in each fit. Metal speciation (i.e., the final fit, or the amount and number of each nickel standard deduced to be contributing to the sample data) can vary drastically when substituting or varying even just one standard as a component. Additionally, when the statistically appropriate number of standards are used (e.g., two to three standards in this case), results can yield similar fits with similar R-factor values. A comprehensive set of LCF results for each soil sample is provided in Table S4 to illustrate this issue. To limit results containing artifacts induced by these problems, the results from the best fits (Table S4) were averaged together to obtain an averaged-based linear combination fitting result and thus average nickel speciation (Table 3). This method buffers the final result (i.e., the final fit) from the wide fluctuations that commonly result from LCF of soil samples with multiple standards. Table S4 and Fig. S5 illustrate how similar fits can be obtained by using different standards.

3. Results

3.1. Physicochemical and mineralogical analysis

Table 1 has the physicochemical properties for the <2 mm soil fraction of the Oregon and Maryland soils. Soil s5t2 is the only sample from Maryland, while all other samples are from Oregon. The pH range of the soils is between 5.6 and 6.9. The clay fractions varied between 20% and 39%, while sand fractions ranged between 25% and 57%. The resulting soil textures ranged between sandy clay loam and clay loam. Nickel concentrations ranged from 1510 mg kg^{-1} to 5970 mg kg^{-1}. Iron concentration is high in several samples but highest in sample s20unt, at 138,600 mg kg^{-1}.

Physicochemical properties of the Jasper Ridge soils have been previously described (Oze et al., 2004). The soils from Jasper Ridge are dominantly Mollisols formed on top of serpentinized peridotite. In both sites (JR3 & COII), nickel concentrations in the soil were less than in the bedrock. Nickel concentrations ranged from 3510 mg kg^{-1} to 2400 mg kg^{-1} in the COII site. The pH of the soils is near neutral and slightly increases with depth, ranging from 6.71 to 6.98. The clay fraction of the JR3 site had the highest concentration of nickel, and the silt fraction the lowest, with about 2900 mg kg^{-1} and 1800 mg kg^{-1}, respectively.

Concentrations of iron, manganese, and nickel for the citrate-dithionite extractions of the clay fractions are listed in Table S2, along with nickel and iron concentrations in serpentine mineral standards from the Katanax fusion digestion. Samples s20unt and s10t2 have the highest percent iron in the clay fraction with 20.2% and 18.4%, respectively. Sample s11unt clay fraction has the lowest amount of iron at 6.4%. For the serpentine mineral standards, Serp96 had the highest iron and nickel concentrations. Nickel can substitute for magnesium in the octahedral layers of silicates, such as serpentine minerals, because its ionic radius is similar to that of magnesium (0.69 Å vs. 0.66 Å, respectively) (Alexander et al., 2007a; Manceau and Calas, 1985).

Table 2 lists the minerals identified by XRD analysis of soil fractions (s5t2, s9t2, s10t2, s11unt, and s20unt; total 17 spectra). The diffractograms from the whole soil, clay, silt and coarse sand fractions, including diffractograms of clay fractions that were citrate-dithionite treated, were analyzed and are shown in Fig. S1. Specific particle size ranges for "sand", "silt", and "clay" are defined in Section 2.2. Serpentine minerals, such as antigorite and lizardite, are commonly present in both the coarse sand and clay fractions of the soils. Talc and quartz are also common. Goethite, hematite, and magnetite are iron oxide minerals found in the soils. Enstatite and pargasite, both chain inosilicate minerals, were found in the XRD patterns of multiple samples. The phyllosilicate clinochlore, which is common in ultramafic rocks, was also identified in multiple samples.

The dithionite treatment of the clay fractions removed iron and manganese oxides and sharpened peaks of silicate minerals (Fig. S1). Serpentine minerals in s5t2, such as antigorite and lizardite, are common. In the dithionite treated (DT) clay fraction of s5t2, the peaks for antigorite, brucite, talc, and quartz are clearer as the goethite peaks have disappeared. The DT clay fraction of s9t2 peaks are mostly due to clinochlore as the broad, smaller iron oxide peaks disappeared.

When the clay fraction of s10t2 was treated with dithionite, the lizardite/antigorite peaks became much clearer, as well as some peaks for clinochlore and quartz. When the clay fraction of s20unt was treated with dithionite, the peaks for goethite and hematite were removed and the silicate-mineral peaks are clearer. After treatment of s11unt clay with dithionite, the lizardite/antigorite peaks are clearer and several of the small, wider peaks from goethite and hematite are gone. The coarse sand fraction of s10t2 was ground in a mortar and pestle from which the clay fraction was retrieved via the centrifugation. This sample was labeled "s10t2 coarse <2 mm" and has peaks for lizardite, quartz, goethite,

Table 1
Physicochemical properties of the Oregon and Maryland Soils.

Sample ID	pH	Sand (%)	Silt (%)	Clay (%)	Texture	Ni (mg kg^{-1})	Fe (mg kg^{-1})	Co (mg kg^{-1})	Cr (mg kg^{-1})	Mn (mg kg^{-1})	Ca (mg kg^{-1})	Mg (mg kg^{-1})	Ca:Mg
s5t2	6.0	25	49	27	Loam	1510	67,900	87	580	1340	631	12,500	0.05
s9t2	6.4	28	33	39	Clay loam	2330	38,700	229	2910	2870	4770	15,000	0.32
s10t2	6.3	57	23	20	Sandy clay loam	4710	46,400	243	2300	2970	936	15,700	0.06
s11unt	5.6	45	31	25	Loam	1660	73,800	100	1870	1620	6160	23,600	0.26
s13t2	6.4	37	30	33	Clay loam	4160	46,300	311	1790	3360	8780	21,900	0.40
s14t2	6.1	43	31	26	Loam	3700	111,000	211	2280	2940	1100	18,300	0.06
s15t2	6.2	56	24	20	Sandy clay loam	2470	38,200	119	1020	1400	919	24,600	0.04
s20unt	6.9	34	27	39	Clay loam	5970	138,600	242	1610	3100	477	13,900	0.03
Average	6.2				Average	3310	70,100	192	1800	2450	2970	18,200	0.15
Median	6.3				Median	3086	57,122	220	1829	2904	1016	16,983	0.06

Table 2
XRD results of soils and soil fractions compiled from diffractograms in Fig. S1.

	Antigorite	Lizardite	Brucite	Talc	Clinochlore	Chlorite	Enstatite	Pargasite	Goethite	Hematite	Magnetite	Quartz
s5t2 clay DT	x	x	x	x								x
s5t2 clay	x	x		x					x			x
s5t2 coarse	x			x								x
s9t2 clay DT					x							x
s9t2 clay					x				x	x		
s9t2 coarse				x	x		x	x				x
s10t2 clay DT	x	x			x		x					x
s10t2 clay	x	x		x			x		x	x		x
s10t2 coarse (ground < 2 μm)		x		x			x		x	x		x
s10t2 coarse	x	x		x			x			x	x	x
s11unt clay DT	x	x										x
s11unt clay	x	x							x	x		x
s11unt coarse	x	x			x		x	x			x	x
s20unt clay DT	x	x		x	x	x						x
s20unt clay	x								x	x	x	
s20unt silt	x	x		x	x		x	x			x	x
s20unt coarse	x	x		x	x		x			x	x	x

enstatite, and hematite (Fig. S1); thus the coarse fraction of s10t2 has sand-sized goethite and hematite iron oxides.

Fig. S2 shows diffractograms of minerals, both natural and synthetic, used as standards for LCF of EXAFS data. COIIbr and JR3br have very similar mineralogy; however, COIIbr contains some magnetite while JR3br displays clear diffraction peaks for lizardite; the JR3br peaks line up consistently with pure serpentine mineral phases Serp96, 185 and 5811. Thus, JR3br is a good sample to use as a lizardite standard for LCF of EXAFS data. Peaks for the nickel-doped minerals magnesium oxalate, magnetite, hematite, goethite, and Ni-Fe LDH all correspond to their correct phases.

Mineralogical data of the Jasper Ridge soils have been previously described (Oze et al., 2004). The serpentinite at Jasper Ridge is composed of mainly lizardite and antigorite (70%), chlorite (15%), talc (10%), magnetite (4%), and chromite (1%). Other minerals include olivine, augite, and enstatite. Nickel in these samples was found in three phases in the JR3 bedrock, including olivine, serpentine, and a nickel-iron metal alloy, probably awaruite. Only soils from sites JR3 and COII were used in the present study. The clay size fraction of the JR3 site is composed of smectite, vermiculite, lizardite, antigorite, clinochlore, and Cr-clinochlorite, with smectite being the most abundant mineral. This mineralogy did not vary significantly at different depths (Oze et al., 2004).

3.2. Particle size fractionation

Fig. 1 shows how the different particle size fractions (sand, silt, and clay) influence nickel speciation in two soil samples, s20unt and s10t2. EXAFS spectra and their Fourier transform (FT) magnitudes are shown in Fig. 1a and b, respectively. The four EXAFS spectra for each soil are from the different particle size fractions, clay, silt, coarse sand, and the whole soil (<2 mm). Fig. 1c shows the LCF results of the whole soil fraction using spectra from each particle size as the components of the fit.

The clay fraction is the dominant component in s20unt, as it accounts for 75% of the nickel species from the whole soil. The s20unt whole soil fraction can be reconstructed using just the clay and silt fractions. However, for s10t2, the distribution of nickel is more homogeneous between particle sizes as both the clay and coarse components contribute about equally to the whole soil spectrum. The clay fraction comprises 54% of nickel while the coarse sand fraction 46%.

3.3. Synchrotron-based data acquisition and analysis

Fig. S3 shows the results of PCA analysis of the soils and indicates that at most four spectra are needed to reconstruct the EXAFS data. This can be determined by visual analysis of the oscillations of components 1–5. Component #4 (blue line) is the last component with discernable oscillations; it has more signal than noise. This method was the most basic, initial way of determining the number of components needed to reconstruct the data. Additionally, a scree plot was employed, where a break in the slope of the scree plot indicates the minimum number of components in the system (Webb, 2005). The components that lie on the linear portion of the plot are probably due to noise versus components that come before the break in the slope of the line that are probably structural (Calvin, 2013). The scree plot has a slight break in the slope at four components (Fig. S3b, inset), which would again indicate that the EXAFS data can be reconstructed with a minimum of four standards. However, the major break in the slope is at two components, which indicates that at minimum two components are necessary to adequately reconstruct the data. Based on these varied results, between two and four components were necessary to reconstruct the data. Further analyses by F-tests provided additional information to determine the number of standards that statistically improved fits.

Table S3 shows a full list of standards considered for LCF of soil EXAFS data, their SPOIL, chi-square, and R-values. Each of the 45 standards in Table S3 is shown in Fig. S4. Of the 45 total standards considered, 27 were selected to use in LCF. Any standard not previously published (references in Table S3) was characterized via shell fitting of the FT EXAFS data to ensure it was accurately prepared. In total, there were 18 spectra previously unpublished and shell fitting results of those 18 spectra are in Table S5.

Table 3 contains the averaged-based results of LCF for soil nickel speciation. Mafic and serpentine related minerals heavily contribute to nickel speciation in many of the soils. On average, mafic and serpentine related minerals contribute 55% of all nickel species for the whole soil fractions, with a range from 16% in s20unt to 83% in s14t2. This indicates that in these topsoils primary serpentine minerals are the important hosts for nickel. Additionally, iron oxides are also consistently important hosts for nickel, with 42% of nickel species related to iron oxides in the whole soil fraction of s10t2. Nickel adsorption to a phyllosilicate (montmorillonite) is also an important component in s15t2 soil, s5t2 soil and s10t2 soil. Manganese oxides are a minor component in several soils; however there are artifacts in the LCF results caused by spectral similarities between birnessite and several of the standards. Discussion is dedicated to manganese oxides in Section 4.3.1, Section 4.4, and in the Supplementary Materials text.

Select LCF graphing results are shown in Fig. 2. The fit for each sample (dotted red line) is labeled with its R-factor that corresponds to the component results in Table S4. The soils have similar major oscillations with differences in the locations of shoulders and beat patterns. Multiple spectra have indentations on the first oscillation at 3.8 Å^{-1}. Samples

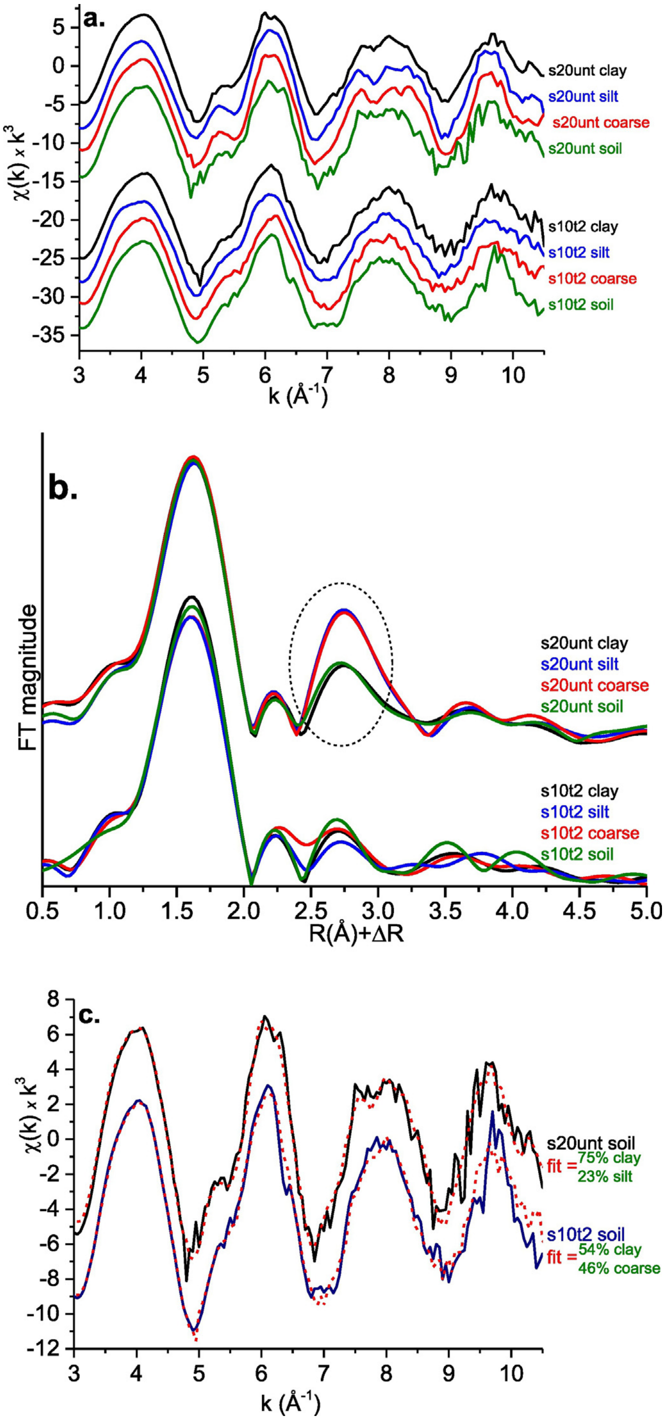

Fig. 1. LCF using particle sizes as components. a.) EXAFS spectra of s20unt and s10t2 samples and b.) Fourier transformed magnitude plots of the EXAFS data. c.) LCF of the soil whole-soil fractions using spectra from their respective particle sizes.

Table 3
Averaged-based results of LCF for soil nickel speciation. These results are the averaged values of fits in Table S4, which reduces over-dependency on any one particular standard. An in-depth discussion of the values reported here, including the influence of false-positive results and mixed metal second shells, is presented in Sections 4.3 and 4.4.

	Mafic & Serpentine Related	Iron oxide	Manganese oxide	Adsorbed to phyllosilicate	Sum
COII 0–2 cm	70%	27%	3%	–	100%
COII 2–5 cm	75%	21%	4%	–	100%
COII 5–8 cm	74%	18%	8%	–	100%
COII 8–11 cm	74%	22%	5%	–	100%
COIIbr	76%	20%	–	–	96%
JR3 0–5 cm	72%	25%	5%	–	102%
JR3 5–15 cm	61%	31%	4%	3%	100%
JR3 15–30 cm	71%	28%	–	–	99%
JR3 30–45 cm	52%	41%	6%	–	98%
JR3br	78%	21%	–	–	99%
s5t2 clay	69%	28%	–	–	97%
s5t2 coarse	59%	38%	–	–	97%
s5t2 soil	52%	13%	9%	24%	98%
s9t2 coarse	69%	31%	–	–	100%
s9t2 soil	52%	–	52%	–	104%
s10t2 clay	51%	29%	22%	–	101%
s10t2 coarse	30%	47%	17%	–	94%
s10t2 silt	42%	47%	–	–	89%
s10t2 soil	23%	42%	–	34%	99%
s11unt clay	83%	15%	–	–	98%
s11unt coarse	96%	–	–	–	96%
s13t2 soil	73%	30%	–	–	103%
s14t2 soil	83%	15%	–	4%	103%
s15t2 soil	46%	16%	7%	32%	101%
s20unt clay	24%	15%	62%	–	101%
s20unt coarse	11%	15%	76%	–	101%
s20unt silt	45%	33%	22%	–	100%
s20unt soil	14%	10%	76%		100%

COII, JR3, s5t2, s9t2, s11unt, s14t2 and s15t2 have this feature. Multiple fitting results for the same sample are presented in Table S4 because even though a lower R-factor statistically indicates a better fit, the fit with the lowest R-factor or appropriate number of standards may miss structurally relevant features of the sample, such as shoulders at 3.8 $Å^{-1}$ or 5.2 $Å^{-1}$. This is illustrated in Fig. S5. Table S4 also contains the results from F-tests (Hamilton tests) for each sample, labeled as "*I*" values. Normally two to three standards were used for LCF based on the results of the F-tests. A 95% confidence interval with the F-Test was employed, and no improvement in any fits was statistically significant by adding four standards. By using this method, there is less than a 5% chance that the improvement in a fit is caused by random variation or noise in the data.

4. Discussion

4.1. Physicochemical and mineralogical analysis

In the Klamath Mountains, the well-drained soils which formed from peridotite yield more free iron oxides than soils which formed from serpentinite (Alexander, 2004). This explains the high iron values in the most oxidized soil samples in this study (e.g., s20unt and s10t2) (Table 1, Table S2). The low Ca:Mg ratios are typical of serpentine soils (Table 1), which have characteristically low Ca:Mg ratios (Burt et al., 2001). The high chromium in the samples comes from chromite, which commonly is present in serpentine soils. Although, in the bulk XRD data, few diffraction peaks for chromite are seen (Fig. S1). Nickel in chromite is tetrahedrally coordinated and has very distinct X-ray absorption pre-edge and edge features not seen in many serpentine soils (Manceau and Calas, 1986).

For the Jasper Ridge soils, site COII was treated with sequential extractions, and the majority of nickel remained in the solid phase. Most of the nickel in the Jasper Ridge site originated from olivine. During serpentinization, the resulting serpentine mineral also contained nickel, and small grains of a nickel-iron alloy (awaruite) were produced. The concentration of nickel increased as other elements weathered and leached out over time (Oze et al., 2004).

Ultramafic Oregon soils have been studied by several researchers (Alexander, 2004; Alexander and DuShey, 2011; Alexander et al., 2007b; Borine, 1983; Burt et al., 2001; Hotz, 1964; Istok and Harward, 1982). Serpentine minerals are considerably more resistant to weathering than olivine and pyroxene (Alexander, 2004), and so their presence in samples in this study is understandable. In some of the more oxidized samples, such as s20unt, the relative abundance of iron

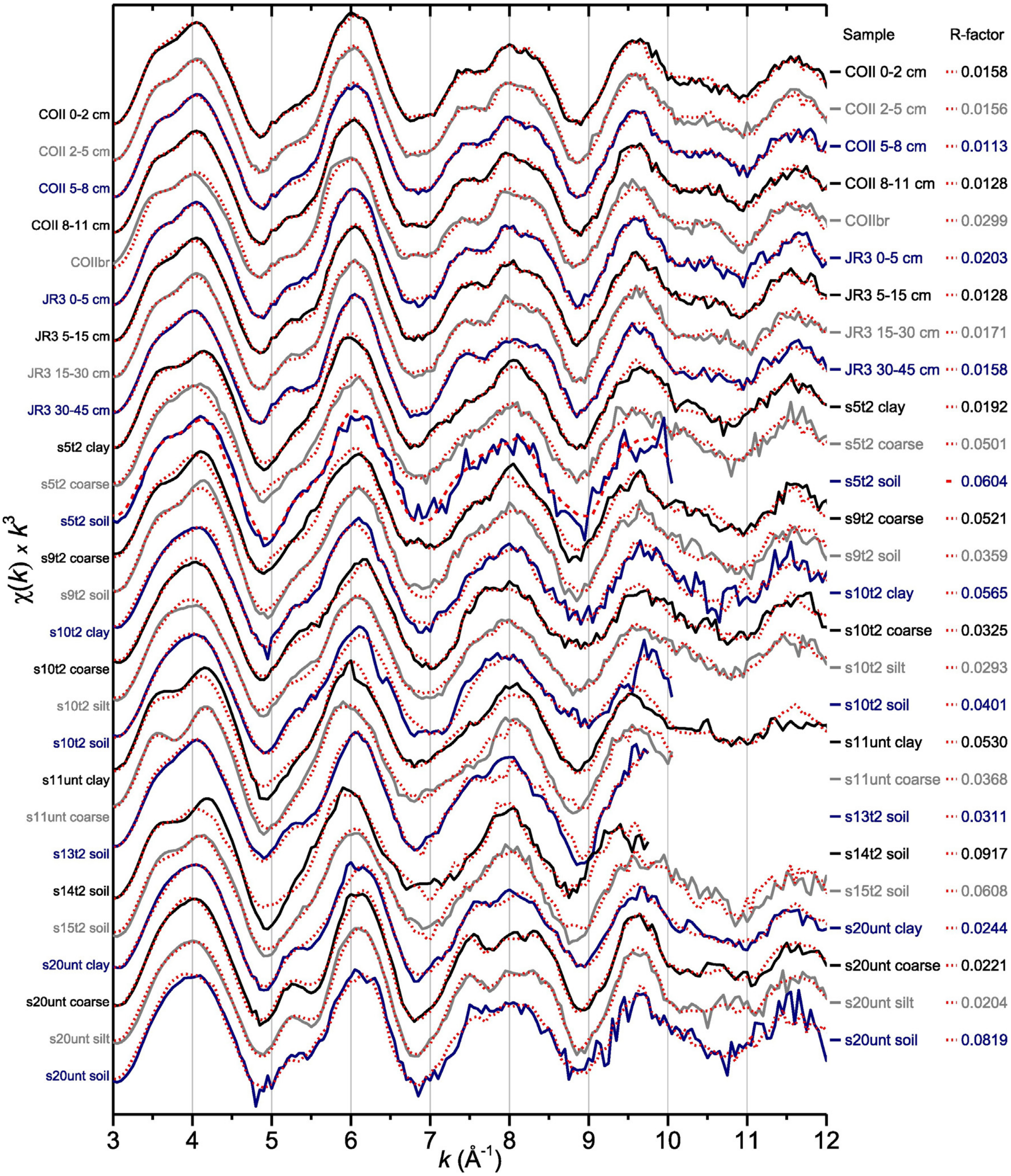

Fig. 2. Select LCF results for serpentine soils and soil fractions. The solid lines indicate the sample data while the dotted red lines indicate the fits. R-factors for the fits displayed in the legend can be linked to the components shown in Table S4, where other comparable fits are also displayed. (For interpretation of the references to color in this figure legend, the reader is referred to the web version of this article.)

oxides versus serpentine minerals is evident especially in the clay fraction (Table 2, Table S2, Fig. S1). Other studies have shown that serpentine minerals in this area had weathered away (Hotz, 1964), but their presence is common in these samples. Serpentine minerals were found to be dominant in the clay fraction of several serpentine soils from other studies in the Klamath Mountains (Burt et al., 2001). In a serpentine soil from Maryland, serpentine minerals were found in the coarse clay and silt fractions but not in the fine clay fraction (Rabenhorst et al., 1982). Serpentine minerals were identified in the clay fraction of the Maryland soil (s5t2) presented here (Fig. S1).

Trevorite is a nickel-iron oxide spinel that can occur in ultramafic rocks and has been identified in this area of the Klamath Mountains (Bird and Weathers, 1975; Hudson and Travis, 1981). Pargasite is in the amphibole group, and thus is an inosilicate mineral. It can occur in altered ultramafic rocks (Anthony et al., 2003). Inosilicates, or chain silicates, can originate in mafic rocks (Schaetzl and Anderson, 2005). Pargasite was identified in the ultramafic rocks of Bear Mountain in the Klamath Mountains in California (Snoke et al., 1981), and it is identified in samples s9t2 coarse, s11unt coarse, and s20unt in this study. In s20unt, the presence of enstatite is understandable because enstatite is an orthopyroxene mineral that is found in similar serpentine soils derived from harzburgite (Alexander, 2004). Nickel not incorporated into iron oxides at the soil profile surface can migrate downward and become enriched into silicate phases (or garnierite) at the bottom of the weathering profile. This enrichment process at the bottom of the profile is a supergene process (Carvalho-E-Silva et al., 2003) and can occur in both nickel sulfide and laterite deposits (Gleeson et al., 2004; Suarez et al., 2011).

4.2. Particle size fractionation

Fig. 1 is the LCF results of two whole soil fractions using particle sizes as components. It illustrates that a significant portion of nickel is located in the clay fraction of s20unt, where 75% of the whole soil EXAFS spectrum can be fit using the clay fraction. Nickel has been shown to accumulate in the clay fraction of serpentine soils (Oze et al., 2004). In s20unt, there is a more pronounced shoulder in both the silt and coarse sand fractions at ~5.3 $Å^{-1}$ and ~7.2 $Å^{-1}$ (Fig. 1a). For s10t2, all four spectra look similar, indicating that nickel species have similar local atomic environments. Fourier transformed spectra of s20unt in Fig. 1b show the second neighbor (the second shell) to nickel is larger in both the coarse sand and silt fractions as compared to the clay and whole soil fractions (dotted circle). A smaller second shell here can indicate a more heterogeneous sorption environment for nickel in the clay fraction. The clay fraction contains higher amounts of iron oxide and phyllosilicates clays, where nickel is likely to be both adsorbed and incorporated in a variety of binding sites. This heterogeneous environment would yield a smaller second shell (smaller amplitude) because of low scattering path degeneracy. Because larger particle size fractions, such as the silt and coarse sand fractions, contain larger, more crystalline minerals, there is more probability for higher path degeneracy and multiple scattering. This would lead to the presence of a larger second shell (larger amplitude) as seen in s20unt Fig. 1b.

This trend, however, does not hold true for s10t2, where all size fractions have similar EXAFS spectra as well as amplitudes in the first and second shells of the FT (Fig. 1a and b). Given the similarities in the EXAFS spectra of all three size fractions in s10t2, it is not unexpected that nickel is more evenly distributed between particle sizes (Fig. 1c). This similarity is most likely because both size fractions contain significant quantities of iron oxides, causing similar nickel species to be present in all size fractions. In s10t2, more nickel is associated with the coarse sand fraction than in s20unt. Sample s10t2 also has a more sandy texture (Table 1), indicating that soil texture plays a role in the differences in nickel speciation for these two samples.

In other studies where nickel was associated with amorphous iron oxides, more than two thirds of total soil nickel was in the clay fraction. However, nickel was less associated with well crystalline iron oxides, and crystallization during pedogenesis was a process that separated nickel from goethite particles (Bani et al., 2009; Bani et al., 2007).

4.3. Synchrotron-based data acquisition and analysis

4.3.1. LCF

Table 3 contains the averaged-based results of LCF carried out on the samples. The results are averages of multiple fits found in Table S4. In the Jasper Ridge COII site, nickel speciation does not change significantly throughout depths. Most samples have features related to mafic and serpentine minerals. This indicates that even in the top layers of the soil, where weathering is most intense, the major species of nickel remain in their primary mineral phases. Different standards consistently created fits with similar R-factors (Table S4). For example, in COII 2–5 cm, Ni-Al Silicate appears in the best fit, but immediately following in the next fit is gibbsite. Those standards were objectively grouped together in the mafic and serpentine group. Iron oxides make up to 18–27% of the total spectra throughout the COII profile. Similar results are found for the JR3 site, with most of the samples exhibiting spectral features related to mafic and serpentine minerals. These results align with the findings in Oze et al., 2004, where the majority of nickel remained in the solid phase. The most recalcitrant nickel is in the silicate minerals. JR3 bedrock (br) is consistently a major component of all samples from the COII and JR sites (Table S4).

JR3br is a critical standard to characterize accurately because of its inclusion as a standard to fit other samples. Diffraction data for JR3br display clear diffraction peaks for lizardite (Section 3.1, Fig. S2). The averaged-based LCF results indicate that nickel in JR3br is 78% mafic and serpentine related and 21% iron oxides. Individual fits of JR3br are shown in Fig. S5 to illustrate the accuracy of the fits at low k. There is no F-test value (Table S4) for this sample because of the 3–7 $Å^{-1}$ k-range used to do LCF of this sample. This range was chosen to focus on characterizing the low k-range with the best accuracy possible and because serpentine mineral standards (e.g., #5811) had more noise at higher k values (e.g., >8 $Å^{-1}$).

Sample s5t2 contains diffraction peaks for serpentine minerals including antigorite and lizardite. The LCF results indicate that a majority of nickel is associated with those phases. In the whole soil fraction, nickel is additionally found to be adsorbed to phyllosilicate clays (montmorillonite). This component is not present in the clay fraction because of the different k-range used. The spectrum from the whole soil had increased noise compared to the spectra from the clay and coarse fractions, so a shorter k-range was necessary (Table S4).

Nickel is also associated with mafic and serpentine minerals in s9t2 (52–69%). Pargasite was found in the diffractogram of s9t2, which is a chain inosilicate mineral. Nickel EXAFS from inosilicate minerals can exhibit features similar to RS birnessite, which was found to compose 52% of the s9t2 whole soil EXAFS spectrum. Section 4.3.3 discusses the cause of this similarity and how it can cause artifacts in LCF results. Thus s9t2 likely has very low contribution from any manganese oxides.

Iron concentrations were high in s10t2 (Table 1, Table S2), and iron oxides comprised a larger LCF percentage in s10t2 than in any other sample on average (Table 3). XRD also indicates that hematite is present in the coarse fraction. Similarly to s5t2, higher noise in the whole soil spectrum reduced the k-range for LCF fitting, and Ni-adsorbed to phyllosilicate (montmorillonite) became an important component in the fit. Enstatite, a chained inosilicate mineral, is present in all fractions (Table 2) and is artificially increasing the manganese oxide percentage in the clay and coarse fractions (see Section 4.3.3).

In s11unt, mafic and serpentine related minerals are the dominant nickel species, which agrees with the diffraction data and the spectral feature at 3.8 $Å^{-1}$ (Fig. 2). At this energy, splitting in the first oscillation of the EXAFS signal occurs, indicating nickel is located in the octahedral sheet of a layered-type hydroxide surrounded by magnesium (see Section 4.3.3). Samples s13t2 and s14t2 also have high amounts of nickel incorporated into mafic and serpentine minerals, with iron oxides contributing 30% and 15% to the sample data, respectively (Table 3). According to elemental data, however, s14t2 has more than twice the total iron in the soil (Table 1) and the second highest amount of iron overall. Thus, concentration measurements do not correlate with nickel speciation. Sample s14t2 has a prominent split in its first oscillation as well, indicating nickel is mostly present in a magnesium-silicate mineral and less so in iron oxides (Fig. 2). Sample s15t2 also has a slight split of the first EXAFS oscillation, indicating a large presence of mafic and serpentine minerals. Additionally in s15t2, nickel is adsorbed to phyllosilicates (montmorillonite), which is indicated as 32% of the average-based nickel species.

Even though RS birnessite (a Ni-manganese oxide standard, Table S3, Fig. S4) was found to be an important component in s20unt by LCF analysis, it is likely that this is an artifact. The sonication method employed disperses clays into solution. Then the silt and sand fractions were rinsed clean with water, removing the manganese oxides which are primarily located in the clay size fraction. The reason that RS birnessite fits so well with the s20unt data is because it has a shoulder at 5.2 $Å^{-1}$ (Fig. S4), just like the s20unt sand and silt fractions. Additionally in s20unt sand and silt fractions, there are truncated oscillations between 7.5 and 8.5 $Å^{-1}$, precisely where the same feature occurs in RS birnessite. These spectral similarities are what give this standard a false positive LCF result. It is more likely that silicates such as enstatite are hosting a significant amount of nickel.

Enstatite is an inosilicate, pyroxene mineral common to mafic rocks. Nickel is a metal cation that can bond the tetrahedral silica chains together. Enstatite was found in the XRD pattern of s20unt coarse and silt fractions (Fig. S1) as was pargasite, another inosilicate mineral.

Trevorite is a Ni-Fe spinel in the magnetite series, and magnetite is identified in the XRD pattern of s20unt silt (Fig. S1). Trevorite is also indicated in Table S4 as a component in several of the fits for the s20unt sample. Thus in s20unt, magnetite is most likely another source of nickel. Additionally, the trevorite spectrum (Fig. S4) also has truncated oscillations between 7.5 and 8.5 Å^{-1}. This similarity further compounds the problem of different standards having similar spectral features (see Section 4.4 for further discussion).

4.3.2. F-tests

F-tests are an aid to determine an appropriate number of standards to use in a linear combination fit (Calvin, 2013). To employ the F-test, the number of independent data points of the sample EXAFS data should be kept the same for each fit. This way multiple fits can be compared where different numbers of standards are used. Artemis software was used to determine the number of independent data points, and then "I" values were determined as in Calvin, 2013. An "I" value is the result of the F-test (Table S4). A 95% confidence level was employed, meaning that for a fit with three standards to be statistically better than a fit with two standards, "I" must be <0.05 (i.e., 5%). The same premise is used to determine if a fit with four standards is statistically better than a fit with three standards and so on. Adding more standards to a linear combination fit almost always reduces the R-factor, so this test provides a quantitative way to determine if the fit improvement is statistically significant or not.

For example in Fit #1 in Table S4, F-tests were carried out on the best fits using two and three standards. Using the R-factor values from the best fits with two and with three standards, the "I" value was calculated. For Fit #1, $I = 0.053$; thus using three standards does not statistically improve the fit because $I > 0.05$. However, for Fit #7, $I = 0.036$, using three standards statistically improved the fit. The same test was done for fits using three and four standards. In no case were four standards found to have "I" values <0.05 versus fits using three or two standards. The F-test results prove that visual inspection of the components and the scree plot (Fig. S3) may not suffice to determine the significant number of standards to include in the fit. Although PCA and the scree plot indicated four standards were necessary to reconstruct the data, the fits do not statistically improve when four standards were added.

Exceptions to this method can be made when structurally important features are not captured. For example, in Fig. S5, fits of s5t2 soil are shown. The F-test ($I = 0.161$, Fit #13, Table S4) determined that s5t2 soil should only need two standards. However, the best fit using two standards (Fit #13, Round #7, R-factor 0.0620) did not capture structurally relevant features. The fit line, although close to the real data, is smoother than the real data and does not follow the structurally relevant shoulders at 3.8 Å^{-1} and 5.2 Å^{-1}. Those shoulders are present because of long range order in the octahedral layers of the minerals antigorite and lizardite, which are found in the diffractograms of s5t2 (Table 2, Fig. S1). Nickel is located in the octahedral sites of these minerals (see Section 4.3.3). Thus, to improve the fit, three standards were used (Fit # 13, Rounds # 1 through 6). Even with the use of three standards, the "best" fit (R-factor 0.0531) is misfit at 3.8 Å^{-1} because it does not follow the slight splitting of the first oscillation. This specific portion of the spectra is critical because the splitting creates a shoulder at 3.8 Å^{-1} and is caused by multiple scattering of light elements in the octahedral layer. Round #1 of Fit #13 has the lowest R-factor but does not conform to important features of the sample spectra, especially at low k-ranges. Fits with R-factors 0.0531 and 0.062 were not included in the averaged-based result (Table 3).

Analysis of the fit at low k-range was also important for s11unt coarse sand (Fig. S5). The fit which most accurately matches the sample at low k actually has a higher R-value (0.0368 vs. 0.0357). These fits were considered to be equivalently good, and both were used to calculate average-based results (Table 3). Sample s13t2 soil in Fig. S5 is problematic because statistics from the F-test show that only two standards yield statistically significant results (Table S4, Fit #22, $I = 0.054$). However, with the inclusion of 30% goethite as a third standard, the fit is improved at 3.8 Å^{-1}, effectively decreasing the shoulder intensity of the fit. Additionally, the shoulder at 5.7 Å^{-1} more accurately matches the sample spectra. Thus, here three standards produce a more appropriate fit than two even though the F-test indicates only two standards should be used.

The fits of s15t2 soil (Fig. S5, Fit #24 in Table S4) have R-factors ranging from 0.0520 to 0.0649. All of these fits replicate the major and minor oscillations and shoulders of the sample spectrum except Round #5 (R-factor = 0.0625). It poorly fits the data at 3.8 Å^{-1}. Between 5 and 5.5 Å^{-1}, the shoulder is also missed, yet a reasonable R-factor value is still produced. Round #5 is an example of how a poor fit can give a reasonable R-factor. It was not included in the average-based result (Table 3). The s10t2 silt fits (Fig. S5, Table S4, Fit # 18) illustrate how different nickel compositions and R-factors can produce similar fits. In Rounds #1–3, different standards are present yet produce similar fits. Round #3 has an R-factor of 0.0476, which is >60% larger than the best fit in Round #1.

4.3.3. Mixed metal second shells

In Fig. 2, the indentation in the first oscillation of multiple samples at 3.8 Å^{-1} indicates the presence of a "light" element, such as magnesium, as a second neighbor to the central absorbing nickel atom in a phyllosilicate or layered hydroxide-type environment. This type of shoulder is commonly present in layered hydroxide octahedra where light elements (e.g., magnesium or aluminum) neighbor "heavier" elements (e.g., zinc or nickel) (Manceau et al., 1987; Manceau et al., 2004). The split of the first oscillation at 3.8 Å^{-1} is caused by light elements in the second coordination shell of the absorbing atom (Manceau et al., 2000). The size of the split is affected by the number of heavy atoms surrounding the central absorber. A higher amount of heavy atoms results in a decrease in the splitting. The split can be used as a diagnostic tool for this type of structural environment in unknown materials (Manceau et al., 2004; Schlegel et al., 2001). The split feature is identifiable in the serpentine minerals standards in this study (Fig. S4). Zn-phyllosilicates have a similar spectral feature to nickel rich serpentine minerals (Ni-phyllosilicates) where light magnesium atoms surround zinc causing the split in the first oscillation (Manceau et al., 2003).

Specific limitations in EXAFS for studying trioctahedral phyllosilicates have been documented (Manceau, 1990). There are *in-and-out* of phase oscillations for magnesium and nickel atoms in the second shell. Nickel can substitute for magnesium because they have similar atomic radii. The presence of magnesium with nickel in the second shell decreases the amplitude of the wave backscattered by the surrounding nickel atoms in such a way that EXAFS cannot separate the contributions of nickel from magnesium (Manceau and Calas, 1986). The addition of silicon at about 3.24 Å may be necessary to fit the second shell data. However, silicon is *in-phase* with nickel oscillations yet magnesium is *out-of-phase*. These *in-and-out* of phase oscillations significantly complicate shell fitting analysis of phyllosilicates. Nickel and iron have similar backscattering phases and amplitudes and cannot be distinguished by EXAFS. Silicon, aluminum, and magnesium as a group and iron and nickel as another group have nearly equal scattering factors and prevent the distinction between atoms in each group based on scattering intensity and phase. Silicon interferes constructively with nickel at low k and increases the total amplitude; however, magnesium interferes destructively and its contribution to the EXAFS spectrum is "subtracted" from that of nickel and silicon atoms (Manceau, 1990).

The EXAFS data of s20unt silt were fit using the crystal structure of enstatite (a chain inosilicate mineral found in this sample), allowing for inclusion of three scatterers in the second shell (Ni, Mg, Si) in a restrained fit (Table S5, Fig. S6). From the FEFF input file, there were 6 Ni-O scattering paths for the first shell at an average of 2.081 Å. The number of scattering paths for the second shell was 9, including 5 total Ni/Mg atoms and 4 Si atoms. The Ni-Mg scattering paths had a range of 2.973 to 3.194 Å. By doping atoms into the FEFF input file, average Ni-Ni and Ni-Mg distances of 3.051 and 3.149 Å, respectively, were determined. The 4 Si scattering paths were between 3.159 and 3.301 Å with an average distance of 3.254 Å. The data show a very close fit to the structure of enstatite (Table S5, Fig. S6).

For the fit, the second shell was broken into three parts, Ni, Mg, and Si, where Ni was substituted for Mg in the FEFF input file. The fit showed very close agreement with the FEFF calculated paths, with fitted values of 3.06 and 3.14 Å for the Ni-Ni and Ni-Mg distances, respectively (Table S5). The fitted distance for Ni-Si scattering was 3.294 Å, which agrees closely with the average FEFF calculated scattering distance of 3.254 Å. The fit was restricted to have equal amounts of Ni/Mg in the second shell and 1.6 times more Si than Ni/Mg, as would be the case for the pure phase mineral.

Constructive and destructive scattering (Fig. S6b) of the nickel, magnesium, and silicon atoms occurs in the second shell. This type of interference has been well documented in layered hydroxides and phyllosilicates (Manceau, 1990). However, it has not been well documented for chained inosilicate minerals like those found in this study. Fig. S6b clearly illustrates the *in-and-out* of phase oscillations which can also cause constructive and destructive interference in inosilicate minerals. In LDHs, this same type of interference is what causes peak truncation between 7 and 9 $Å^{-1}$ (Scheinost and Sparks, 2000; Siebecker et al., 2014). Ni-Al LDH fits into s20unt silt (Table S4, Fit #27, Round #3), which contains enstatite, because of the peak truncation and double peaks present between 7 and 9 $Å^{-1}$. EXAFS spectra of inosilicate minerals can have similar features of a Ni-Al layered double hydroxide.

4.4. XRD vs. EXAFS

Fig. 3 illustrates a complication that can arise while using LCF to analyze EXAFS spectra of soils. Fig. 3a compares the XRD spectrum of the s20unt silt fraction (black line) versus the XRD spectrum of a typical Ni-Al LDH (red line). This being the silt fraction of s20unt, all clays have been removed from the sample via sonication (Section 2.2). Thus, the spectrum is of particles only in the 25–45 μm range. Vast differences in the XRD spectra are evident, with the Ni-Al LDH notably having much fewer and broader peaks. The crystallinity of the silt fraction is noted by the multitude of sharp diffraction peaks, which are identified explicitly in Fig. S1 and Table 2. Although not all of those phases are nickel-rich (e.g., quartz), the silicate and layered hydroxide minerals (such as clinochlore, enstatite, pargasite, talc, lizardite, and forsterite) are potential locations for nickel.

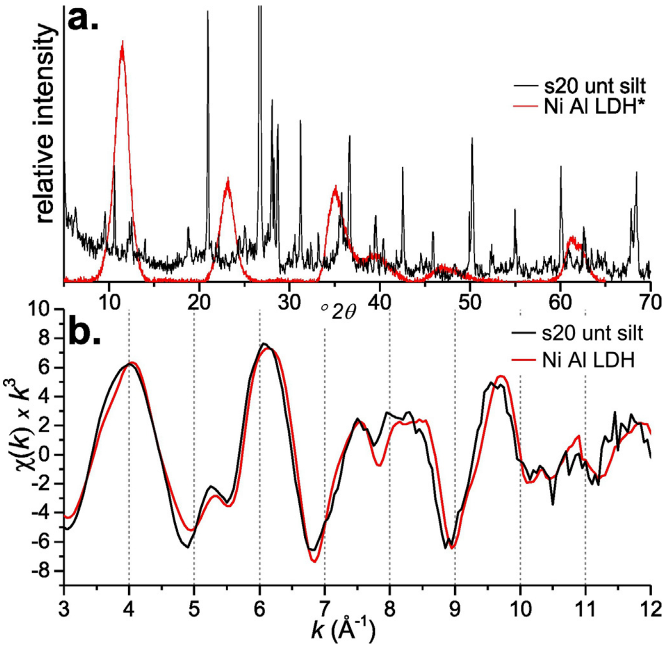

Fig. 3. a.) XRD spectra of s20unt silt and Ni-Al LDH*, where * indicates a typical XRD pattern of a Ni-Al LDH [see (Peltier et al., 2006) for comparison]. b.) The EXAFS comparison of s20unt silt vs. Ni-Al LDH. Although these two spectra have very distinct diffraction patterns, their EXAFS indicate almost identical local atomic environments for nickel. Mineralogy for s20unt silt is identified in Fig S1. Because the layered minerals present in s20unt silt have similar octahedral structure as Ni-Al LDH the resulting EXAFS are also similar, thus producing a “false positive” result in LCF.

The diffractograms show that the mineralogy of the two samples is very distinct. The comparison of their EXAFS spectra, however, shows clear similarities and hence similar local nickel environments in both samples (Fig. 3b). The samples have different mineralogy but similar local atomic environment of nickel. The phase and amplitude of both EXAFS spectra are similar for two samples with such different mineralogy. This similarity, however, should not be surprising because many nickel-rich minerals in serpentine soils, e.g., lizardite, are layered silicate minerals with nickel located in the octahedral layer along with the lighter element magnesium. Magnesium can have a similar effect as aluminum (Section 4.3.3). The Ni-Al LDH is a layered hydroxide mineral with both nickel and aluminum in the octahedrally-coordinated (hydroxide) layer. Because nickel is located in the octahedral layer and surrounded by light elements, such as magnesium and aluminum, in both serpentine minerals and Ni-Al LDH, it logical that the spectra are quite similar. The light elements cause dampening of the upward peak at ca 8.2 $Å^{-1}$ in the LDH structure when compared to single metal layered hydroxides (Scheinost and Sparks, 2000).

This type of structural similarity between standards can lead to a false positive result when reporting LCF results. This is why the LCF results reported in this paper (Table 3) are done in an average-based approach of multiple fits: to avoid over-dependence on one specific standard. The Ni-Al LDH standard was grouped into the “Mafic and Serpentine Related” standards (Section 2.3) because of the structural similarities between LDH and lizardite. Often, lizardite is used as a crystal structure model when shell fitting EXAFS data of LDHs (Scheinost and Sparks, 2000).

LCF results of s20unt silt (Fit #27, Table S4) with similar statistical results indicate the major nickel components are nickel silicates and serpentine minerals. Additionally, with respect to the formation of LDH in serpentine soils, other researchers have identified at 8 $Å^{-1}$ a strong double oscillation for nickel adsorbed to phyllomanganates (Fan and Gerson, 2011). In Fig. S4, the random stacked birnessite (RS Birn) contains a double peak between 7 and 9 $Å^{-1}$ that is similar to Ni-Al LDH, which is another reason why the LDH fits well into LCF and why manganese oxides were determined to be a major component of the s20unt silt and coarse fraction (Table 3). Even after sonication, when all clay sized manganese oxides were removed from both coarse and silt particle size fractions, one of the major components determined by LCF were manganese oxides (Table 3). This is a false positive result, and in this particle size the major nickel species are the silicate minerals.

4.5. Conclusions

In this study, when the percent of iron oxides from LCF results are plotted against total iron concentration from digestion data, there is no correlation in the plot. Similarly, when the percent of mafic and serpentine related minerals from LCF results are plotted against total magnesium concentration, there is no correlation in the plot. Because serpentine minerals are high in magnesium, this correlation would be reasonable to find. The lack of correlation indicates that total elemental concentration of a specific metal is not an indicator of the major nickel species in the soil. X-ray diffraction and particle size separation provided information on which minerals can potentially host nickel. Crystallographic data assisted in selecting appropriate standards for LCF of EXAFS data.

Differences in soil texture were related to different nickel speciation for several particle size fractionated samples. Sample s10t2 has more nickel located in the coarse sand fraction than s20unt (Section 4.2, Fig. 1). In s20unt, 75% of the nickel could be attributed to the clay fraction. These results correlate to the soil texture of both samples, where s10t2 is a sandy clay loam with 57% sand and 20% clay, and s20unt is a clay loam with 34% sand and 39% clay (Table 1).

Nickel speciation determined by LCF in the Jasper Ridge soils did not vary significantly with depth. Oze et al., 2004 found that mineralogy in these soils did not vary significantly at different depths. Differences in nickel species between soils can be readily identified by the splitting of the first oscillation at 3.8 Å^{-1}. However, this split is not explicitly linked to metal concentrations in the soil. For example, s14t2 had the second highest iron content (111,000 mg kg^{-1}), thus it would be expected that iron oxides would be a major component in this sample. However, even with the high iron content, there is a split in the first oscillation of the EXAFS (Fig. 2), and LCF determined that layered silicate minerals were the major species (Table 3, Table S4).

Regardless of location, several minerals were commonly identified by XRD. Those minerals were lizardite, antigorite, clinochlore, talc, enstatite, and goethite. Other common iron oxides were hematite and magnetite. In addition to enstatite, another inosilicate mineral (pargasite) was identified in several samples.

Based on LCF of EXAFS data, nickel was often associated with primary serpentine minerals, many of which have a layered octahedral hydroxide and tetrahedral silicon sheets. Primary serpentine minerals are the most important hosts for nickel. Nickel is also likely associated with inosilicate minerals, such as enstatite. In inosilicate minerals, which are common in mafic rocks, a variety of metal cations can balance the negative charge of the silicate tetrahedra chains and bond the chains together. Lastly, nickel was also commonly associated with iron oxides such as goethite, hematite and ferrihydrite. Other researchers have also found that iron oxides, such as goethite, serpentine minerals and talc were the most common nickel bearing minerals in ultramafic soils (Echevarria et al., 2006).

Multiple caveats involved with LCF of EXAFS data using synthetic standards were illustrated. Large variation in calculated percent composition when slightly modifying standards used in the fit is a common problem. A method of averaging the best fits together to obtain a result that is buffered from these large variations was presented. Additionally, different standards can yield statistically similar fits. Chemically different standards can exhibit similar EXAFS features because of structural similarities. Even the best fit can miss important structural features, such as shoulders caused by multiple scattering of light elements. Precautions while using this method include considering other chemical and mineralogical data to aid in selecting standards and appropriate fitting results.

The F-test is an underutilized tool in the literature for LCF of EXAFS data for metal speciation in soils. Its use here proved that although visual inspection of the principal components and scree plot indicated four standards may be necessary to reconstruct the data, the fits were not statistically improved by using four or even sometimes three standards. Additionally, by developing a sonication method, it was possible to show that nickel species vary depending on particle size, in the sand, silt or clay fraction. An illustration and discussion were presented on how false positive results can occur in LCF. The most appropriate linear combination fit depends on the researcher making informed decisions based on additional mineralogical, chemical, and particle size information for each sample.

Acknowledgements

Dr. Siebecker is grateful for University of Delaware graduate and dissertation fellowships and for the Donald L. and Joy G. Sparks graduate fellowship. Additionally, he is grateful for assistance from Jerry Hendricks, Chris Oze, Brian McCandless, Cathy Olsen, Clara Chan, Ted Peltier, Mike Zhu, and Kaumudi Pandya. This research was supported in part by the National Science Foundation Experimental Program to Stimulate Competitive Research grant number EPS-0814251. Use of the NSLS was supported by the US Department of Energy under contract No. DE-AC02-98CH10886. Use of the Stanford Synchrotron Radiation Lightsource is supported by the U.S. Department of Energy under contract No. DE-AC02-76SF00515. The SSRL Structural Molecular Biology Program is supported by the DOE Office of Biological and Environmental Research, and by the National Institutes of Health and National Institute of General Medical Sciences (including P41GM103393). The contents of this publication are solely the responsibility of the authors and do not necessarily represent the official views of NIGMS or NIH.

Appendix A. Supplementary data

Supplementary data to this article can be found online at http://dx.doi.org/10.1016/j.geoderma.2017.03.008.

References

Alexander, E.B., 2004. Serpentine soil redness, differences among peridotite and serpentinite materials, Klamath mountains, California. Int. Geol. Rev. 46, 754–764.

Alexander, E.B., Coleman, R.G., Keeler-Wolf, T., Harrison, S.P., 2007a. Serpentine Geoecology of Western North America: Soils, Geology, and Vegetation. Oxford University Press.

Alexander, E.B., DuShey, J., 2011. Topographic and soil differences from peridotite to serpentinite. Geomorphology 135, 271–276.

Alexander, E.B., Ellis, C.C., Burke, R., 2007b. A chronosequence of soils and vegetation on serpentine terraces in the Klamath mountains, USA. Soil Sci. 172, 565–576.

Amelung, W., Zech, W., 1999. Minimisation of organic matter disruption during particle-size fractionation of grassland epipedons. Geoderma 92, 73–85.

Amelung, W., Zech, W., Zhang, X., Follett, R.F., Tiessen, H., Knox, E., Flach, K.W., 1998. Carbon, nitrogen, and sulfur pools in particle-size fractions as influenced by climate. Soil Sci. Soc. Am. J. 62, 172–181.

Anthony, J.W., Bideaux, R.A., Bladh, K.W., Nichols, M.C., 2003. Handbook of Mineralogy, Mineralogical Society of America, Chantilly, VA 20151-1110, USA. http://www.handbookofmineralogy.org/.

Antic-Mladenovic, S., Rinklebe, J., Frohne, T., Stark, H.J., Wennrich, R., Tomic, Z., Licina, V., 2011. Impact of controlled redox conditions on nickel in a serpentine soil. J. Soils Sediments 11, 406–415.

Bani, A., Echevarria, G., Mullaj, A., Reeves, R., Morel, J.L., Sulce, S., 2009. Nickel hyperaccumulation by *Brassicaceae* in serpentine soils of Albania and northwestern Greece. Northeast. Nat. 16, 385–404.

Bani, A., Echevarria, G., Sulce, S., Morel, J.L., Mullai, A., 2007. In-situ phytoextraction of Ni by a native population of *Alyssum murale* on an ultramafic site (Albania). Plant Soil 293, 79–89.

Bird, J.M., Weathers, M.S., 1975. Josephinite: specimens from the earth's core? Earth Planet. Sci. Lett. 28, 51–64.

Borine, R., 1983. Soil Survey of Josephine County, Oregon. US Department of Agriculture, Natural Resources Conservation Service, Washington, D.C., p. 168.

Burt, R., Fillmore, M., Wilson, M.A., Gross, E.R., Langridge, R.W., Lammers, D.A., 2001. Soil properties of selected pedons on ultramafic rocks in Klamath Mountains, Oregon. Commun. Soil Sci. Plant Anal. 32, 2145–2175.

Calvin, S., 2013. XAFS for Everyone. CRC Press.

Carvalho-E-Silva, M.L., Ramos, A.Y., Tolentino, H.C.N., Enzweiler, J., Netto, S.M., Alves, M., 2003. Incorporation of Ni into natural goethite: an investigation by X-ray absorption spectroscopy. Am. Mineral. 88, 876–882.

Cheng, C.H., Jien, S.H., Izuka, Y., Tsai, H., Chang, Y.H., Hseu, Z.Y., 2011. Pedogenic chromium and nickel partitioning in serpentine soils along a toposequence. Soil Sci. Soc. Am. J. 75, 659–668.

Colin, F., Nahon, D., Trescases, J.J., Melfi, A.J., 1990. Lateritic weathering of pyroxenites at Niquelandia, Goias, Brazil - the supergene behavior of nickel. Econ. Geol. Bull. Soc. Econ. Geol. 85, 1010–1023.

Crystal-Impact (2012) Match! 1.11d, Crystal Impact GbR, http://www.crystalimpact.com/match/Default.htm, info@crystalimpact.com.

Decarreau, A., Colin, F., Herbillon, A., Manceau, A., Nahon, D., Paquet, H., Trauthbadaud, D., Trescases, J.J., 1987. Domain segregation in Ni-Fe-Mg-smectites. Clay Clay Miner. 35, 1–10.

Doelsch, E., Basile-Doelsch, I., Rose, J., Masion, A., Borschneck, D., Hazemann, J.L., Saint Macary, H., Borrero, J.Y., 2006. New combination of EXAFS spectroscopy and density fractionation for the speciation of chromium within an andosol. Environ. Sci. Technol. 40, 7602–7608.

Echevarria, G., Massoura, S.T., Sterckeman, T., Becquer, T., Schwartz, C., Morel, J.L., 2006. Assessment and control of the bioavailability of nickel in soils. Environ. Toxicol. Chem. 25, 643–651.

Fan, R., Gerson, A.R., 2011. Nickel geochemistry of a Philippine laterite examined by bulk and microprobe synchrotron analyses. Geochim. Cosmochim. Acta 75, 6400–6415.

Gaudin, A., Decarreau, A., Noack, Y., Grauby, O., 2005. Clay mineralogy of the nickel laterite ore developed from serpentinised peridotites at Murrin Murrin, Western Australia. Aust. J. Earth Sci. 52, 231–241.

Gee, G.W., Or, D., 2002. Particle-size analysis. In: Dane, J.H.A.T., C. (Eds.), Methods of Soil Analysis Part 4 Physical Methods. Soil Science Society of America Book Series, Madison, Wisconsin, USA.

Gimbert, L.J., Haygarth, P.M., Beckett, R., Worsfold, P.J., 2005. Comparison of centrifugation and filtration techniques for the size fractionation of colloidal material in soil suspensions using sedimentation field-flow fractionation. Environ. Sci. Technol. 39, 1731–1735.

Gleeson, S.A., Herrington, R.J., Durango, J., Velasquez, C.A., Koll, G., 2004. The mineralogy and geochemistry of the Cerro Matoso SA Ni laterite deposit, Montelibano, Colombia. Econ. Geol. 99, 1197–1213.

Hamilton, W.C., 1965. Significance tests on the crystallographic R factor. Acta Crystallogr. 18, 502–510.

Holmgren, G.G.S., 1967. A rapid citrate-dithionite extractable iron procedure. Soil Sci. Soc. Am. Proc. 31, 210–211.

Hotz, P.E., 1964. Nickeliferous laterites in southwestern Oregon and northwestern California. Econ. Geol. 59, 355–396.

Hseu, Z.Y., 2006. Concentration and distribution of chromium and nickel fractions along a serpentinitic toposequence. Soil Sci. 171, 341–353.

Hudson, D.R., Travis, G.A., 1981. A native nickel-heazlewoodite-ferroan trevorite assemblage from Mount Clifford, Western Australia. Econ. Geol. 76, 1686–1697.

Istok, J.D., Harward, M.E., 1982. Influence of soil-moisture on smectite formation in soils derived from serpentinite. Soil Sci. Soc. Am. J. 46, 1106–1108.

Jackson, M.L., 1985. Soil Chemical Analysis - Advanced Course. second ed. University of Wisconsin, Madison, WI.

Kahle, M., Kleber, M., Torn, M.S., Jahn, R., 2003. Carbon storage in coarse and fine clay fractions of illitic soils. Soil Sci. Soc. Am. J. 67, 1732–1739.

Loeppert, R.P., Inskeep, W.P., 1996. Iron. In: Bigham, J.M. (Ed.), Methods of Soil Analysis. Part 3. Chemical Methods. Soil Science Society of America and American Society of Agronomy, 677 S. Segoe Rd., Madison, WI 53711, USA.

Manceau, A., 1990. Distribution of cations among the octahedra of phyllosilicates - insight from EXAFS. Can. Mineral. 28, 321–328.

Manceau, A., Calas, G., 1985. Heterogeneous distribution of nickel in hydrous silicates from New Caledonia ore-deposits. Am. Mineral. 70, 549–558.

Manceau, A., Calas, G., 1986. Nickel bearing clay minerals: 2. Intracrystalline distribution of nickel - an X-ray absorption study. Clay Miner. 21, 341–360.

Manceau, A., Llorca, S., Calas, G., 1987. Crystal-chemistry of cobalt and nickel in lithiophorite and asbolane from New-Caledonia. Geochim. Cosmochim. Acta 51, 105–113.

Manceau, A., Marcus, M.A., Tamura, N., Proux, O., Geoffroy, N., Lanson, B., 2004. Natural speciation of Zn at the micrometer scale in a clayey soil using X-ray fluorescence, absorption, and diffraction. Geochim. Cosmochim. Acta 68, 2467–2483.

Manceau, A., Schlegel, M.L., Musso, M., Sole, V.A., Gauthier, C., Petit, P.E., Trolard, F., 2000. Crystal chemistry of trace elements in natural and synthetic goethite. Geochim. Cosmochim. Acta 64, 3643–3661.

Manceau, A., Tamura, N., Celestre, R.S., MacDowell, A.A., Geoffroy, N., Sposito, G., Padmore, H.A., 2003. Molecular-scale speciation of Zn and Ni in soil ferromanganese nodules from loess soils of the Mississippi Basin. Environ. Sci. Technol. 37, 75–80.

Massoura, S.T., Echevarria, G., Becquer, T., Ghanbaja, J., Leclere-Cessac, E., Morel, J.L., 2006. Control of nickel availability by nickel bearing minerals in natural and anthropogenic soils. Geoderma 136, 28–37.

North, P.F., 1976. Towards an absolute measurement of soil structural stability using ultrasound. J. Soil Sci. 27, 451–459.

Oorts, K., Vanlauwe, B., Recous, S., Merckx, R., 2005. Redistribution of particulate organic matter during ultrasonic dispersion of highly weathered soils. Eur. J. Soil Sci. 56, 77–91.

Oze, C., Fendorf, S., Bird, D.K., Coleman, R.G., 2004. Chromium geochemistry in serpentinized ultramafic rocks and serpentine soils from the Franciscan Complex of California. Am. J. Sci. 304, 67–101.

Peltier, E., Allada, R., Navrotsky, A., Sparks, D.L., 2006. Nickel solubility and precipitation in soils: a thermodynamic study. Clay Clay Miner. 54, 153–164.

Rabenhorst, M.C., Foss, J.E., Fanning, D.S., 1982. Genesis of Maryland soils formed from serpentinite. Soil Sci. Soc. Am. J. 46, 607–616.

Raine, S.R., So, H.B., 1994. Ultrasonic dispersion of soil in water - the effect of suspension properties on energy-dissipation and soil dispersion. Aust. J. Soil Res. 32, 1157–1174.

Schaetzl, R.J., Anderson, S., 2005. Soils: Genesis and Geomorphology. Cambridge University Press.

Scheinost, A.C., Sparks, D.L., 2000. Formation of layered single- and double-metal hydroxide precipitates at the mineral/water interface: a multiple-scattering XAFS analysis. J. Colloid Interface Sci. 223, 167–178.

Schlegel, M.L., Manceau, A., Charlet, L., Hazemann, J.-l. (2001) Adsorption mechanisms of Zn on hectorite as a function of time, pH, and ionic strength. Am. J. Sci. 301, 798–830.

Schmidt, M.W.I., Rumpel, C., Kogel-Knabner, I., 1999. Evaluation of an ultrasonic dispersion procedure to isolate primary organomineral complexes from soils. Eur. J. Soil Sci. 50, 87–94.

Siebecker, M., Li, W., Khalid, S., Sparks, D., 2014. Real-time QEXAFS spectroscopy measures rapid precipitate formation at the mineral–water interface. Nat. Commun. 5.

Snoke, A.W., Quick, J.E., Bowman, H.R., 1981. Bear Mountain igneous complex, Klamath Mountains, California: an ultrabasic to silicic cale-alkaline suite. J. Petrol. 22, 501–552.

Sohi, S.P., Mahieu, N., Arah, J.R.M., Powlson, D.S., Madari, B., Gaunt, J.L., 2001. A procedure for isolating soil organic matter fractions suitable for modeling. Soil Sci. Soc. Am. J. 65, 1121–1128.

Solomon, D., Fritzsche, F., Tekalign, M., Lehmann, J., Zech, W., 2002. Soil organic matter composition in the subhumid Ethiopian highlands as influenced by deforestation and agricultural management. Soil Sci. Soc. Am. J. 66, 68–82.

Suarez, S., Nieto, F., Velasco, F., Martin, F.J., 2011. Serpentine and chlorite as effective Ni-Cu sinks during weathering of the Aguablanca sulphide deposit (SW Spain). TEM evidence for metal-retention mechanisms in sheet silicates. Eur. J. Mineral. 23, 179–196.

Webb, S.M., 2005. SIXpack: a graphical user interface for XAS analysis using IFEFFIT. Phys. Scr. T115, 1011–1014.

Yamaguchi, N.U., Scheinost, A.C., Sparks, D.L., 2002. Influence of gibbsite surface area and citrate on Ni sorption mechanisms at pH 7.5. Clay Clay Miner. 50, 784–790.

Yang, X.M., Drury, C.F., Reynolds, W.D., MacTavish, D.C., 2009. Use of sonication to determine the size distributions of soil particles and organic matter. Can. J. Soil Sci. 89, 413–419.

Supplementary Materials for

Nickel Speciation in Several Serpentine (Ultramafic) Topsoils via Bulk Synchrotron-Based Techniques

Matthew G. Siebecker[*,a], Rufus L. Chaney[b], Donald L. Sparks[a,c]

[a] University of Delaware, Delaware Environmental Institute (DENIN), Newark, DE, 19716, USA.
[b] United States Department of Agriculture, Adaptive Cropping Systems Laboratory, Beltsville, MD, 20705, USA.
[c] University of Delaware, Department of Plant and Soil Sciences, Newark, DE, 19716, USA.
*Correspondence to: mgs@udel.edu

Contents:

MATERIALS AND METHODS

RESULTS

TABLES

FIGURES

REFERENCES

MATERIALS AND METHODS

Synthesis of Mineral Standards

Nickel-iron layered double hydroxides (LDHs) with ratios of 2:1 and 10:1 Ni:Fe were synthesized and their diffraction peaks are typical for LDHs (Figure S2). A coprecipitation method was followed (Saiah et al., 2009) however with no hydrothermal treatment. For the 2:1 ratio, 0.5 M nickel(II) nitrate hexahydrate and 0.25 M iron(III) nitrate nonahydrate solutions were mixed together and then added dropwise to a solution of 0.5 M NaOH and 0.5 M Na_2CO_3 at pH 11 while rapidly stirring. 100 mL of Ni/Fe solution was mixed with 100 mL of the 0.5 M $NaOH/Na_2CO_3$ solution. The combined solution was mixed mechanically at pH 11. A pH stat with 1 M Na_2CO_3 to maintain the pH was used until pH stabilized at less than 2 mL of base addition per hour. The precipitates were collected via centrifugation, washed 4-5 times with 18.2 megohm water and freeze dried.

Four iron oxides, including 2-line ferrihydrite, goethite, hematite and magnetite were synthesized (Schwertmann and Cornell, 1991), except for adding 1% nickel(II) nitrate hexahydrate on a molar basis to the iron solutions. X-ray diffractograms of iron oxide species confirmed their identity (Figure S2). Ni-Fe LDH and iron oxide phases were dissolved in concentrated HCl, diluted and analyzed by ICP-OES to determine nickel content. The ferrihydrite, goethite, hematite, magnetite and 2:1 Ni/Fe LDH contained 0.4%, 0.6%, 0.6%, 0.4%, and 31.7% nickel by weight, respectively.

The coprecipitation of magnesium-nickel oxalate solid solutions was also carried out (Packter and Omomo, 1984), ranging from 0% nickel to 60% nickel substitution for magnesium. Additionally a 100% nickel oxalate sample was prepared. For XAS and LCF, only the 5% nickel magnesium oxalate sample was used, as XAS indicated identical spectra (in both k and r space) for 5%, 60% and 100% Ni in Ni-Mg oxalate. The Ni-Mg Oxalate peaks, where 5% nickel is incorporated into magnesium oxalate, agree well with diffractograms of crystalline magnesium oxalate (Lakshmi Reddy et al., 2014; Mohandes et al., 2010). Nickel rich magnesium oxalate was included in this study because the weathering of serpentinite rock by biotic processes has shown that secondary magnesium oxalate crystals containing both iron and nickel were found (Wilson et al., 1981; Wilson et al., 1980).

Synthesis of the acid birnessite (“Acid Birn”) sample was described in (Centofanti et al., 2012) and nickel sorption was carried out in a 500 mL slurry of 4 g acid birnessite and 0.01 M nickel(II) nitrate hexahydrate. The slurry reacted over night while maintaining pH at ca 7, with the final pH being 6.86. The sample was washed 3x with deionized water at pH 6.9 and freeze dried. ICP analysis of HCl digested mineral showed an average nickel content of 333 mg Ni/g product. Synthesis of random stacked birnessite (“RS birnessite”) is described in (Zhu et al., 2010) and was done in the same way as the “NiTr” sample in that paper.

Preparation of nickel sorbed to humic acid was previously described (Centofanti et al., 2012). Preparation of “Kaolinite pH 6” and “Kaolinite pH 7.5” was carried out previously (Peltier et al., 2010). The nickel citrate sample was a solid phase salt purchased from Alfa Aesar and diluted to ca 9% w/w with boron nitride for XAS data acquisition. Serpentine mineral standards were obtained from the University of Delaware’s mineralogical supply (serpentine mineral sample numbers 96, 185, and 5811). Sample JR3 bedrock is from Oze et al., 2004. The nickel foil spectrum was from the foil collection at beamline X18B at the NSLS. The awaruite sample was of the variety Josephinite and obtained from Josephine Creek, Oregon through excaliburmineral.com. References for all previously characterized and published EXAFS standards are in Table S3. Table S5 contains the EXAFS shell fitting results of the 18 new standards presented in this paper.

Synchrotron Beamline Characteristics

All EXAFS data presented in this paper are nickel K-edge EXAFS spectra. Synchrotron beamlines used in this study are described in Table S1. The electron beam storage ring energy was 2.5–2.8 GeV with a maximum beam current of 300 mA at the National Synchrotron Light Source (NSLS). The electron beam energy was 3 GeV with a maximum beam current of 300mA at the Stanford Synchrotron Radiation Lightsource (SSRL). Gas ionization chambers (where used) were filled with either nitrogen or argon or a mix of both gases to obtain ca 10-20% beam absorption in I_0, and 50-70% absorption in I_1 and I_2. The Lytle detector (where used) was filled with argon gas. Harmonic X-ray elimination was achieved by detuning the monochromators ca 30-35%, unless Kirkpatrick-Baez mirrors were used, where typically beam energy >24 keV does not pass through the mirror setup. Additionally, beamline 4-1 at SSRL is equipped with a harmonic rejection mirror at 22 keV. X-ray filters were always used when collecting data in fluorescence mode (i.e., either 3 or 6 absorption length Z-1 cobalt filters). When necessary, one to five layers of aluminum foil were used to preferentially attenuate iron fluorescence to reduce Fe K-beta fluorescence interference.

For bulk-EXAFS, the sub-2 mm fraction of serpentine soil and other soil fractions were powdered via mortar and pestle and placed in sample plastic holders of ca 1.5 mm thickness. All samples were placed in the beam path at 45° to the beam and 45° to the detector. Nickel K-edge EXAFS spectra were collected from ca 200 eV below the absorption edge to ca 12.5 k-space. Sufficient scans were taken to increase signal to noise ratio, generally between 5 and 15 scans depending on nickel and iron concentrations. Scans were calibrated with a nickel foil using the peak of its first derivative at 8333 eV.

PCA, TT, SPOIL, LCF and F-test

Principal component analysis (PCA) of EXAFS data (Wasserman et al., 1999) was carried out using Sixpack software (Webb, 2005). Sixpack also was used to perform target transformation (TT) of standards to yield SPOIL values (Malinowski, 1978). SPOIL values were considered in a similar fashion as others (McNear et al., 2007). Standards were considered for LCF based their SPOIL, Chi square and R-values. Eigenvalues were also determined (Malinowski, 1977) and plotted in a scree plot. The chi-square value is a sum of the squared differentials, and the R-value is a measure of the percent misfit (Webb, 2005). In addition to the scree plot, the visual appearance of components were examined to assist in determining how many were enough to account for the structure in the EXAFS spectra (Calvin, 2013).

PCA and a scree plot of the eigenvalues of each component were used to assist in determining the appropriate number of components to use for LCF. The 14 most diverse EXAFS spectra of serpentine soils and soil fractions (of 27 total spectra) were used in PCA and the scree plot. The most diverse spectra were selected for PCA to avoid bias that would have resulted from having multiple similar spectra. These 14 spectra were chosen based on visual distinctions in their EXAFS spectra.

Athena X-ray absorption spectroscopy (XAS) data processing software (Ravel and Newville, 2005) was used to carry out linear combination fitting (LCF) analyses of EXAFS data from whole soil and particle size separated fractions using a set of standards. In addition to the scree plot and appearance of components, F-tests (or Hamilton tests) (Hamilton, 1965) were carried out on all LCF results while varying the number of standards to determine if adding a new component statistically improved the LCF result (Calvin, 2013; Downward et al., 2007). F-tests assisted in determining the appropriate numbers of standards to use in LCF and were carried out using a regularized lower incomplete beta function calculator (Soper, 2015). X-ray diffraction and elemental data of the soils were also used to assist in interpreting LCF results and in selecting the most appropriate standards to fit sample spectra.

Fitting EXAFS Spectra of Nickel Standards

Table S5 contains the EXAFS shell fitting results of the 18 new standards presented in this paper. In general, fits were constrained as much as possible to reduce the number of fitted variables. Where appropriate, i.e., when best fit did not have the least number of necessary variables, a Hamilton test was used to test fit improvement if more fitting parameters were added (Calvin, 2013). This was done using a Regularized Lower Incomplete Beta Function Calculator. The following practices were employed: for changes in Reff (delta R), an isotropic expansion-contraction term (alpha-Reff) was employed in Artemis where appropriate for cubic crystal structures. This method can reduce the multiple delta R values to a single variable for all paths (Kelly et al., 2008). Delta R values were also grouped together for atoms of similar Z-values (e.g., Ni, Fe) which are also located at similar distances to the absorbing atom (Ni). If fits resulted in delta R values greater than 0.1 Å (e.g., Ni-in ferrihydrite and in goethite), this can be attributed to a local Ni-octahedron distortion in the iron oxide structure used to calculate the scattering paths. In those cases, individual delta-R values were used.

Delta-E values, i.e., the difference between the theoretical scattering path E0 and that of the data, were constrained to be the same for all paths. The Mean Square Relative Displacement (MSRD, σ^2) term, which describes the thermal and statistical disorder, was constrained by grouping MSRD values of similar atomic type and/or bond length (Kelly et al 2008, Calvin, 2013). For example, the MSRD values of nickel and/or iron atoms of second or third metal shells (e.g., Ni-foil, awaruite, and iron oxides) were generally constrained together when possible, based on overlapping MSRD values when fitted independently or when doing so improved the fit to physically realistic values. When necessary, e.g., for disordered structures such as ferrihydrite or fits with local atomic disorder caused by doping (e.g., perhaps in Ni-goethite sample), individual sigma-squared values had to be used. Fits where focused multiple scattering was important used the same changes in path length and MSRD values as their corresponding single-scattering path (Calvin, 2013).

The awaruite fit was constrained to reduce the number of independent variables using a nickel foil crystal structure as a starting point. Coordination numbers for higher shells were set relative to that of the first shell based on the CIF of nickel metal. The sigma squared disorder terms were linked together for shells of similar distance to the absorber. Delta R values were also constrained together to maintain the cubic structure of nickel metal as much as possible. The MRSD value for the second shell in ferrihydrite was constrained to be 3 times that of the Ni-O value in order to obtain realistic coordination numbers. In general, the values for MSRD become larger with increasing bond length (Kelly et al 2008), so this constraint is reasonable for this amorphous solid.

Crystal information files (CIF) files were used to calculate scattering paths for each spectrum. The following papers have associated CIF files that can be found on the American Mineralogy Crystal Structure Database: hematite (Finger and Hazen, 1980); Ni-foil and awaruite (Suh et al., 1988) (nickel metal); goethite (Gualtieri and Venturelli, 1999); Ni-Fe

LDH, Ni-kaolinite pH 7.5, Serp96, Serp5811, Serp185, JR3 BR (Mellini and Viti, 1994) (lizardite); magnetite (O'Neill and Dollase, 1994); ferrihydrite (Jansen et al., 2002); Ni-acid birnessite, RSB pH 7 (Post and Veblen, 1990); Ni-kaolinite pH 6 (Saalfeld and Wedde, 1974) (gibbsite); Ni-Mg-Oxalate, Ni citrate, Ni humic acid (Soleimannejad et al., 2007) (Mn-oxalate, “lindbergite”). The Ni-citrate sample was also fit with Earlandite (Na-Citrate) (Herdtweck et al., 2011) and yielded large first shell oxygen CN (ca 8.5); S20unt silt (Carlson et al., 1988) (enstatite). To calculate theoretical scattering paths between Ni-O and Ni-metal shells, nickel atoms and individual atoms were substituted in the FEFF input file (i.e., nickel atoms were doped into the crystal structure). For example in lizardite, nickel was substituted for magnesium in the octahedral layer and silicon was only included in the fit where appropriate (e.g., with Ni kaolinite at pH 7.5, where a silicated Ni-Al layered double hydroxide was expected and did form). The scattering paths for nickel and iron at similar interatomic distances (e.g., in iron oxides) are not distinguishable because both atoms are very similar in atomic weight, thus the scattering paths are listed in Table S5 as Ni/Fe.

RESULTS

Shell fitting of Nickel-Manganese Oxide Standards

Nickel adsorbed to random stacked birnessite (“RS birnessite”, Table S5, Table S3) was found to be an important component for multiple samples (Table S4). The RS birnessite is a triclinic birnessite where sorption should only occur at edge sites via bidentate binuclear bonding on edge sites (double corner, DC) or tridentate edge sharing (TE) complexes. Because triclinic birnessite should be vacancy-free in the manganese octahedral layer, charge comes from substitution of Mn^{3+} for Mn^{4+} and sorption mainly occurs at edge sites (Peacock and Sherman, 2007b). Manganese scattering at 3.05 Å for the first shell is the distance expected for Ni sorbing to edges via tridentate-edge sharing complex and is seen in this sample.

A triple corner sharing complex (TC) occurs when nickel sorbed to a layer vacancy site in the manganese octahedral layers (Drits et al., 2007; Lafferty et al., 2010; Manceau et al., 2002). Manganese shells at ca 3.08 and 3.48 Å are attributed to Ni sorption at edge site (ca 3.08 Å), which is via a tridentate corner sharing complexes (TE) (Peacock and Sherman, 2007b; Zhu et al., 2010) . For Ni-Mn shell on layered hexagonal birnessite, 3.5 Å is what you would expect for Ni sorption over vacancy site (Peacock and Sherman, 2007b). Ni sorption at vacancy sites in the Mn-octahedral layer or on edge site (triple corner, TC, and double corner DC) respectively) have Ni-Mn distances of 3.48 Å (Zhu et al., 2010), making them difficult to distinguish in R-space. However the EXAFS data show clear differences between TC and DC dominated sorption samples, with TC having split oscillation at 6 and 8 $Å^{-1}$, and at high surface loading the DC bonding becomes dominant sorption mechanism (Manceau et al., 2007). To obtain a reasonable fit for the RS birnessite sample, two manganese paths were necessary, and two paths at ca 2.47 and 3.05 Å were found as expected.

Ni-Mn scattering at 2.9 Å is the expected distance for nickel atoms incorporated into octahedral layer (Peacock and Sherman, 2007a; Peacock and Sherman, 2007b) and there are no distances like this in RS birnessite. However, in the Ni-Acid birnessite sample a small contribution (CN 1.2) of Ni-Mn scattering at this distance is evident. The Ni-Acid birnessite was not found to be an important component in the LCF (Table S4) and thus nickel incorporated into the octahedral later of birnessite is not an important component in these serpentine soils.

Shell fitting of Nickel-Iron Oxide Standards

In a natural goethite sample, the Ni-O distances were found to be 1.98 Å and 2.12 Å with coordination numbers (CN) of 2.2 and 4.3. The Ni-Fe distances were 3.05 Å (CN 1.7), 3.21 Å (CN 1.9), and Ni-Fe 3.73 Å (CN 0.8). In a synthetic goethite, the Ni-O distances were 1.98 Å (CN 2.8) and 2.12 Å (CN 4) and the Ni-Fe distances were 3.00 Å (CN 2.8), 3.17 Å (CN-3.2), and lastly 3.60 Å (CN-0.5) (Carvalho-E-Silva et al., 2003). In another study, (Singh et al., 2002) nickel-iron distances were similar to or shorter than those for iron in goethite: Ni-O 2.06 Å, Ni-Fe 2.99 Å -3.02 Å, Ni-Fe 3.16 Å -3.19 Å, and Ni-Fe 4.03 Å. However, nickel EXAFS of goethite in another study (Fan and Gerson, 2011) showed two main peaks, one at 2.03 Å for O and the second for Fe at 3.03 Å and 3.28 Å (just 1 peak for both Fe atoms). Nickel-doped goethite also indicate two main peaks in the FT data, with Ni-O at 2.060 Å and Ni-Fe/Ni at 2.96 Å and 3.137 Å. The Ni-O distance is similar to that found by Singh et al 2002, while the Ni-Fe/Ni distance at 2.96 Å is slightly shorter that Ni-Fe found by Singh et al 2002. The distance of 3.137 Å perhaps indicates some impurities of $Ni(OH)_2$ are present.

In a nickel synthetic hematite, Ni-Fe distances were 2.90-2.92 Å, Ni-Fe 3.41 Å -3.42 Å and Ni-Fe 3.66 Å -3.67 Å. Nickel replaced iron and no separate nickel phases like NiO or $Ni(OH)_2$. The first shell had two oxygen paths each with CN 3, one at 1.97 Å -1.98 Å and the other at 2.09 Å -2.1 Å (Singh et al., 2000). In nickel-doped hematite, the Ni-O CN was 5.6 at 2.052 Å, indicating just one O shell at about the average Ni-O distance found in Singh et al 2000. The Ni-Fe paths at further distances (2.951 Å, 3.712 Å, and 5.052 Å) are similar to the Fe-Fe distances determined by the FEFF paths based on Finger and Hazen, 1980 (2.969 Å, 3.701 Å and 5.035 Å), indicating incorporation of nickel into the hematite structure.

Distances for nickel-doped magnetite (Ni-O, Ni-Fe, Ni-Fe, 2.056 Å, 2.974 Å and 3.482 Å, respectively) agree well with the FEFF calculated scattering distances (2.039 Å, 2.944 Å, 3.452 Å) of hematite based on the CIF file by O’Neill and Dollase 1994. The Ni-O scattering path found in nickel doped ferrihydrite indicate shorter Ni-O distance than predicted, perhaps due to the nickel octahedra not being distorted in the amorphous ferrihydrite. Ni-Fe/Ni scattering paths in nickel doped ferrihydrite indicate large heterogeneity in nickel boding to iron, suggesting good incorporation of nickel in ferrihydrite.

Supporting Tables and Figures

Table S1. *Synchrotron beamline characteristics.*

Beamline	Technique	Monochromator	X-ray detector types	approximate spot size (horizontal x vertical)
NSLS X11A	Bulk EXAFS	Si (111)	Lytle	5x1mm
NSLS X11B	Bulk EXAFS	Si (111)	Lytle	5x1mm
SSRL 4-1	Bulk EXAFS	Si(220)	13-element germanium array	5x1mm
SSRL 9-3	Bulk EXAFS	Si(220)	100 - element germanium array	5x1mm
SSRL 11-2	Bulk EXAFS	Si(220)	30 - element germanium array	5x1mm

Table S2. *Citrate-dithionite and Katanax fusion elemental data. Iron, manganese and nickel concentrations from citrate-dithionite extractions of soil clay fractions are shown here. Additionally, iron and nickel concentrations from Katanax fusion digestion of serpentine minerals # 5811, 185, and 96 are also shown.*

Sample Name	Fe mg kg^{-1}	% Fe	Mn mg kg^{-1}	Ni mg kg^{-1}
s5t2 clay	94900	9.5	1460	1420
s9t2 clay	101100	10.1	3430	1300
s10t2 clay	184300	18.4	4980	4830
s11unt clay	63500	6.4	2290	925
s20unt clay	202500	20.2	3100	5190
Serp5811	15100	1.5	-	829
Serp185	9900	1	-	1180
Serp96	31200	3.1	-	1950

Table S3. *EXAFS standards considered for LCF of serpentine soils and soil fractions.* ***Bold text indicates samples used for LCF.*** *Non-bold text samples were excluded for use in LCF but evaluated by Target Transformation. The labels for each standard and abbreviations used in this work are shown here. SPOIL values were determined from target transformation, and chi square and R-values of each standard are also listed. Chi square, R-value and SPOIL values were determined using a k-range of 3-12 Å^{-1} with 3 components, although further testing was carried out using k-ranges of 3-10 and 3-12 Å^{-1} with both 3 and 4 components. These values are representative of and similar to other results with different k-ranges and number of components. The source of each standard is also listed. Standards are listed in same order as in Figure S4 (top-to-bottom). Standards in "italics" were not used for LCF after considering their SPOIL, chi square and R-values, or because of resemblance to other standards (e.g., "Kaolinite pH 7.5" is very similar to "Montmorillonite pH 7.5").*

Total #	For LCF	Standard	Chi Sq	R-value	SPOIL	Name in Figure S4	Description	source & description
1	**1**	**Hematite pH 6.85 dry**	**376**	**0.18**	**5.1**	**"Hem pH7 dry"**	**Iron Oxide**	**(Arai, 2008); nickel sorbed to hematite, wet paste**
2	**2**	**Hematite pH 6.85**	**287**	**0.15**	**4.2**	**"Hem pH7"**	**Iron Oxide**	**(Arai, 2008); nickel sorbed to hematite, air dried**
3	**3**	**Goethite pH 6.68**	**263**	**0.12**	**6.8**	**"Goe pH7"**	**Iron Oxide**	**(Arai, 2008); nickel sorbed to goethite, wet paste**
4	**4**	**Ferrihydrite pH 6.89**	**102**	**0.06**	**3.6**	**"Ferri pH7"**	**Iron Oxide**	**(Arai, 2008); nickel sorbed to ferrihydrite, wet paste**
5	**5**	**Ferrihydrite pH 5.92**	**228**	**0.11**	**6.0**	**"Ferri pH6"**	**Iron Oxide**	**(Arai, 2008); nickel sorbed to ferrihydrite, wet paste**
6	**6**	**Ferrihydrite pH 5.09**	**305**	**0.12**	**4.6**	**"Ferri pH5"**	**Iron Oxide**	**(Arai, 2008); nickel sorbed to ferrihydrite, wet paste**
7	—	*δ - (Hydrous) Manganese Oxide*	*698*	*0.23*	*8.2*	*"NiMnO$_2$"*	*n.a.*	*(Zhu et al., 2010); nickel sorption on delta MnO$_2$ at pH 4. Nickel sorbed to vacancy sites.*
8	—	*Acid Birnessite*	*532*	*0.22*	*7.7*	*"A Birn"*	*n.a.*	*This work*
9	**7**	**Random Stacked Birnessite**	**99**	**0.05**	**2.6**	**"RS Birn"**	**Manganese Oxide**	**(Zhu et al., 2010); & This work; nickel sorbed to random stacked birnessite at pH 7**
10	**8**	**Triclinic Birnessite**	**271**	**0.17**	**3.8**	**"NiTC Birn"**	**Manganese Oxide**	**(Zhu et al., 2010); nickel on triclinic birnessite at pH 7. Nickel sorbed to edge and vacancy sites.**
11	—	*Kaolinite pH 6*	*597*	*0.23*	*9.3*	*"Kao pH6"*	*n.a.*	*(Peltier et al., 2010) & this work*
12	—	*Kaolinite pH 7.5*	*233*	*0.09*	*1.5*	*"Kao pH 7.5"*	*n.a.*	*(Peltier et al., 2010) & this work*
13	—	*Vermiculite pH 6*	*115*	*0.06*	*4.2*	*"Verm pH6"*	*n.a.*	*(Peltier et al., 2010)*
14	—	*Vermiculite pH 7.5*	*115*	*0.06*	*1.7*	*"Verm pH7.5"*	*n.a.*	*(Peltier et al., 2010)*
15	**9**	**Montmorillonite pH 6**	**93**	**0.04**	**2.8**	**"Mont pH6"**	**Adsorbed to Phyllosilicate**	**(Peltier et al., 2010)**
16	**10**	**Montmorillonite pH 7.5**	**131**	**0.06**	**1.7**	**"Mont pH7.5"**	**Layered Hydroxide**	**(Peltier et al., 2010)**
17	**11**	**Nickel Aluminum Layered Double Hydroxide**	**200**	**0.09**	**1.9**	**"NiAl LDH"**	**Layered Hydroxide**	**(Peltier et al., 2006)**
18	**12**	**Nickel Iron Layered Double Hydroxide**	**416**	**0.13**	**1.3**	**"NiFe LDH"**	**Layered Hydroxide**	**This work**
19	**13**	**Nickel Aluminum Silicate**	**570**	**0.14**	**1.6**	**"NiAl Silicate"**	**Layered Hydroxide**	**(Ford et al., 1999)**
20	**14**	**Nickel Silicate**	**367**	**0.10**	**0.9**	**"Ni Silicate"**	**Layered Hydroxide**	**(Scheinost and Sparks, 2000)**
21	—	*Nickel on Amorphous Silica*	*1124*	*0.18*	*2.0*	*"Am Silica"*	*n.a.*	*(Scheinost and Sparks, 2000)*

22	**15**	**Alpha Nickel Hydroxide**	**1037**	**0.23**	**2.2**	**α-Ni(OH)$_2$**	**Layered Hydroxide**	**(Scheinost and Sparks, 2000)**
23	—	*Beta Nickel Hydroxide*	*2686*	*0.35*	*3.0*	*β-Ni(OH)$_2$*	*n.a.*	*(Scheinost and Sparks, 2000)*
24	**16**	**Ni-Mg Oxalate**	**331**	**0.14**	**4.4**	**"NiMg Ox$_{(s)}$"**	**n.a.**	**This work**
25	—	*Nickel Citrate$_{(s)}$*	*104*	*0.06*	*2.5*	*"Citrate"*	*n.a.*	*This work*
26	**17**	**Nickel sorbed to Humic Acid**	**127**	**0.08**	**3.0**	**"Humic Acid"**	**n.a.**	**This work**
27	**18**	**Nickel sorbed to Gibbsite**	**185**	**0.07**	**5.3**	**"Gibbsite"**	**Layered Hydroxide**	**(Yamaguchi et al., 2002)**
28	**19**	**Serpentine mineral #96**	**333**	**0.16**	**3.6**	**"Serp 96"**	**Serpentine (layered silicate)**	**This work**
29	**20**	**Serpentine mineral #185**	**233**	**0.13**	**0.4**	**"Serp 185"**	**Serpentine (layered silicate)**	**This work**
30	**21**	**Serpentine mineral #5811**	**449**	**0.19**	**3.2**	**"Serp 5811"**	**Serpentine (layered silicate)**	**This work**
31	**22**	**JR3 bedrock**	**20**	**0.01**	**0.9**	**"JR3br"**	**Serpentine, layered hydroxide & Iron Oxide**	**This work**
32	—	*Sulfate*	*1341*	*0.61*	*11.6*	*"Sulfate"*	*n.a.*	*(McNear et al., 2007)*
33	**23**	**Trevorite**	**221**	**0.07**	**1.0**	**"Trevorite"**	**Iron Oxide**	**(McNear et al., 2007)**
34	—	*Violarite*	*1615*	*0.66*	*6.1*	*"Violarite"*	*n.a.*	*(McNear et al., 2007)*
35	—	*Gaspeite*	*1060*	*0.45*	*7.0*	*"Gaspeite"*	*n.a.*	*(McNear et al., 2007)*
36	—	*Godlevskite*	*2108*	*0.80*	*16.4*	*"Godlevskite"*	*n.a.*	*(McNear et al., 2007)*
37	—	*Heazlewoodite*	*356*	*0.24*	*7.9*	*"Heaz."*	*n.a.*	*(McNear et al., 2007)*
38	**24**	**Goethite**	**281**	**0.11**	**3.4**	**"Goethite"**	**Iron Oxide**	**This work**
39	**25**	**Ferrihydrite**	**202**	**0.09**	**3.5**	**"Ferrihydrite"**	**Iron Oxide**	**This work**
40	**26**	**Hematite**	**1149**	**0.35**	**3.5**	**"Hematite"**	**Iron Oxide**	**This work**
41	**27**	**Magnetite**	**2760**	**0.42**	**3.3**	**"Magnetite"**	**Iron Oxide**	**This work**
42	—	*Ni Foil*	*26923*	*0.99*	*25.1*	*"Ni Foil"*	*n.a.*	*This work*
43	—	*Awaruite*	*8895*	*0.97*	*22.3*	*"Awaruite"*	*n.a.*	*This work*
44	—	*FeMn Nodule*	*4960*	*0.57*	*3.7*	*"FeMn Nod."*	*n.a.*	*(Peacock and Sherman, 2007a)*
45	—	*NiO*	*12952*	*0.74*	*4.5*	*"NiO"*	*n.a.*	*(McNear et al., 2007)*
		mean	**1721**	**0.25**	**5.1**			
		median	**333**	**0.14**	**3.6**			

***Table S4.** A comprehensive list of all LCF results of serpentine soils and soil fractions. F-test results shown in column "I" that are marked with an asterisk*, such as s5t2 soil and s13t2 soil, denote where obvious fit improvement was made by using three standards whilst the F-test determined two standards appropriate. All LCF results presented here were used to create the average nickel composition results in Table 3 except for the following samples where stated rounds were omitted (s5t2 soil, rounds # 1 and 7; s13t2 soil round # 2; s15t2 soil round # 5.*

Fit #	Sample	k range fit	*"I"*	Figure #	Round #	R-factor	Component 1		Component 2		Component 3		Sum
1	COII 0-2 cm	3 to 12	0.053	2	1	0.0158	JR3br	77%	RS Birn	24%	-	-	101%
					2	0.0166	JR3br	90%	NiAl Silicate	9%	-	-	99%
					3	0.0167	JR3br	78%	Gibbsite	20%	-	-	98%
					4	0.0167	JR3br	87%	NiAl LDH	15%	-	-	102%
					5	0.0168	JR3br	87%	Trevorite	12%	-	-	99%
					6	0.0172	JR3br	74%	Ferri pH 7	29%	-	-	103%
					7	0.0181	JR3br	87%	Goethite	13%	-	-	100%
					8	0.0184	JR3br	84%	Goe pH 7	17%	-	-	101%
2	COII 2-5 cm	3 to 12	0.063	2	1	0.0156	JR3br	91%	NiAl Silicate	9%	-	-	101%
					2	0.0157	JR3br	78%	Gibbsite	21%	-	-	99%
					3	0.0161	JR3br	88%	Trevorite	13%	-	-	100%
					4	0.0166	JR3br	80%	RS Birn	22%	-	-	102%
					5	0.0167	JR3br	89%	NiAl LDH	15%	-	-	103%
3	COII 5-8 cm	3 to 12	0.090	2	1	0.0113	JR3br	86%	NiAl LDH	17%	-	-	103%
					2	0.0117	JR3br	76%	RS Birn	25%	-	-	101%
					3	0.0127	JR3br	91%	NiAl Silicate	9%	-	-	100%
4	COII 8-11 cm	3 to 12	0.164	2	1	0.0128	JR3br	91%	NiAl Silicate	9%	-	-	100%
					2	0.0130	JR3br	88%	Trevorite	12%	-	-	100%
					3	0.0133	JR3br	89%	NiAl LDH	14%	-	-	103%
					4	0.0137	JR3br	81%	RS Birn	21%	-	-	102%
5	COIIbr	3 to 12	0.532	2	1	0.0299	JR3br	91%	Serp 185	6%	-	-	97%
					2	0.0306	JR3br	96%	-	-	-	-	96%
6	JR3 0-5 cm	3 to 12	0.126		1	0.0195	JR3br	83%	Trevorite	18%	-	-	101%
				2	2	0.0203	JR3br	88%	NiAl Silicate	13%	-	-	101%
					3	0.0207	JR3br	84%	NiAl LDH	21%	-	-	105%
					4	0.0230	JR3br	75%	RS Birn	28%	-	-	103%
					5	0.0245	JR3br	97%	Magnetite	6%	-	-	103%
					6	0.0277	JR3br	89%	Goethite	14%	-	-	102%
7	JR3 5-15 cm	3 to 12	0.036	2	1	0.0128	JR3br	71%	Trevorite	16%	Goethite	13%	100%
					2	0.0129	JR3br	67%	RS Birn	21%	Trevorite	13%	101%
					3	0.0135	JR3br	66%	Trevorite	18%	Mont. pH 6	17%	101%
					4	0.0136	JR3br	76%	Goethite	13%	NiAl Silicate	11%	100%
					5	0.0139	JR3br	86%	NiAl Silicate	10%	Magnetite	5%	101%
8	JR3 15-30 cm	3 to 12	0.087	2	1	0.0171	JR3br	85%	NiAl Silicate	15%	-	-	100%
					2	0.0181	JR3br	79%	Trevorite	20%	-	-	100%
9	JR3 30-45 cm	3 to 12	0.031	2	1	0.0158	JR3br	55%	Trevorite	25%	Ferrihydrite	18%	98%
					2	0.0164	JR3br	54%	Trevorite	23%	RS Birn	22%	99%
					3	0.0167	JR3br	58%	Trevorite	27%	Goethite	13%	98%
					4	0.0169	JR3br	76%	NiAl Silicate	18%	Magnetite	6%	99%
10	JR3br	3 to 7	n/a	S5	1	0.0072	Ferri pH6	43%	Serp 5811	38%	NiAl Silicate	20%	100%
				S5	2	0.0114	Serp 5811	56%	NiAl Silicate	23%	NiFe LDH	19%	98%
11	s5t2 clay	3 to 12	0.038		1	0.0185	JR3br	43%	Gibbsite	38%	Goethite	16%	97%
				2	2	0.0192	Gibbsite	38%	JR3br	38%	Ferri pH 6	23%	98%
12	s5t2 coarse	3 to 12	0.059	2	1	0.0501	JR3br	68%	Goethite	29%	-	-	99%
					2	0.0558	JR3br	85%	Hematite	14%	-	-	99%
13	s5t2 soil	3 to 10	*0.161	S5	1	0.0531	Mont. pH 6	45%	RS Birn	33%	Serp 5811	27%	105%
				S5	2	0.0553	Gibbsite	49%	Serp 5811	34%	Magnetite	13%	96%
				S5	3	0.0557	RS Birn	46%	Serp 5811	29%	Gibbsite	26%	100%
				S5	4	0.0564	Mont. pH 6	66%	Serp 5811	31%	Magnetite	7%	104%
				S5	5	0.0589	Mont. pH 6	55%	Gibbsite	37%	Magnetite	5%	97%
				2 & S5	6	0.0604	Gibbsite	52%	Ferri pH 5	29%	Magnetite	12%	93%
				S5	7	0.0620	Mont. pH 6	66%	Gibbsite	32%	-	-	98%

14	s9t2 coarse	3 to 12	0.094	2	1	0.0521	JR3br	88%	Hematite	12%	-	-	101%
15	s9t2 soil	3 to 12	0.039	2	1	0.0359	RS Birn	52%	Gibbsite	28%	Serp 96	24%	104%
16	s10t2 clay	3 to 12	0.123	2	1	0.0565	Gibbsite	49%	Hem pH7	48%	-	-	97%
					2	0.0630	RS Birn	65%	Serp 185	40%	-	-	105%
					3	0.0728	JR3br	81%	Hematite	22%	-	-	103%
17	s10t2 coarse	3 to 12	0.012	2	1	0.0325	RS Birn	51%	Serp 185	24%	Hematite	24%	99%
					2	0.0377	JR3br	44%	Hematite	27%	Goethite	25%	96%
					3	0.0448	Gibbsite	32%	Goethite	30%	Hematite	26%	88%
18	s10t2 silt	3 to 12	0.037	2 & S5	1	0.0293	JR3br	53%	Goethite	28%	Hematite	13%	95%
				S5	2	0.0455	Goethite	41%	Gibbsite	26%	Serp 96	22%	88%
				S5	3	0.0476	Goethite	36%	Gibbsite	36%	Hematite	13%	85%
19	s10t2 soil	3 to 10	0.147	2	1	0.0401	Mont. pH 6	68%	Hem pH7	33%	-	-	101%
					2	0.0412	Mont. pH 6	70%	Goe pH 7	29%	-	-	99%
					3	0.0413	Hem pH7	60%	Gibbsite	37%	-	-	98%
					4	0.0498	JR3br	71%	Hematite	30%	-	-	101%
20	s11unt clay	3 to 12	0.086	2	1	0.0530	JR3br	61%	Gibbsite	35%	-	-	95%
					2	0.0553	JR3br	78%	Serp 5811	23%	-	-	101%
21	s11unt coarse	3 to 10	0.111	S5	1	0.0357	Serp 185	53%	Gibbsite	46%	-	-	99%
				2 & S5	2	0.0368	Gibbsite	55%	Serp 5811	38%	-	-	92%
22	s13t2 soil	3 to 10	*0.054	2 & S5	1	0.0311	Serp 5811	40%	NiAl Silicate	33%	Goethite	30%	103%
				S5	2	0.0442	Serp 5811	57%	NiAl Silicate	45%	-	-	102%
23	s14t2 soil	3 to 10	0.220	2	1	0.0917	Serp 96	57%	Ferri pH 6	45%	-	-	102%
					2	0.0928	Serp 185	77%	JR3br	28%	-	-	105%
					3	0.0968	Serp 185	87%	Mont. pH 6	18%	-	-	105%
					4	0.0970	Serp 96	56%	JR3br	44%	-	-	100%
24	s15t2 soil	3 to 12	0.019	S5	1	0.0520	Mont. pH 6	48%	JR3br	35%	Serp 96	21%	104%
				S5	2	0.0549	Mont. pH 6	59%	Serp 96	22%	Ferri pH5	21%	102%
				S5	3	0.0588	Mont. pH 6	52%	Serp 96	31%	Ferrihydrite	20%	103%
				2 & S5	4	0.0608	Serp 96	36%	Ferrihydrite	33%	Gibbsite	30%	98%
				S5	5	0.0625	JR3br	43%	Serp 96	31%	Ferrihydrite	29%	104%
				S5	6	0.0649	Serp 96	36%	RS Birn	36%	Gibbsite	27%	100%
25	s20unt clay	3 to 12	0.035	2	1	0.0244	RS Birn	66%	Gibbsite	22%	Hematite	11%	99%
					2	0.0236	RS Birn	59%	JR3br	33%	Hematite	12%	104%
26	s20unt coarse	3 to 12	0.106	2	1	0.0221	RS Birn	72%	Trevorite	30%	-	-	102%
					2	0.0250	RS Birn	80%	NiAl Silicate	21%	-	-	101%
27	s20unt silt	3 to 12	0.030	2	1	0.0204	RS Birn	43%	Trevorite	34%	Gibbsite	20%	97%
					2	0.0209	Ni silicate	37%	Gibbsite	36%	Hem pH 7	26%	100%
					3	0.0236	JR3br	43%	NiAl LDH	39%	Trevorite	23%	105%
					4	0.0238	RS Birn	44%	Trevorite	35%	JR3br	21%	100%
28	s20unt soil	3 to 12	0.164	2	1	0.0819	RS Birn	64%	Goe pH 7	37%	-	-	101%
					2	0.0899	RS Birn	79%	Serp 185	25%	-	-	104%
					3	0.0927	RS Birn	71%	Gibbsite	25%	-	-	96%
					4	0.0932	RS Birn	82%	Serp 96	19%	-	-	102%
					5	0.1012	RS Birn	85%	Trevorite	12%	-	-	97%

Table S5. *EXAFS shell fitting results of the 18 new standards presented in this paper (as indicated by "this work" in Table S3) and sample s20unt silt.* ***R factor*** *is the absolute misfit between data and theory [R = Sum(|data - fit|^2) / Sum(|data|^2)] employed by FEFFIT;* N_{idp} *is the number of independent points;* N_{var} *is the number of fitted variables;* χ^2 *is the chi-square value;* χ^2_n *is the reduced-chi-square value;* ***CN*** *is the coordination number;* R_{eff} *in Å is the effective path length determined from the crystal information file (CIF) used to create the scattering paths, and is half if the path length prior to calculating R;* ***R*** *is the interatomic distance in Å;* σ^2 *is the Debye–Waller factor in Å^2;* ΔE *is the energy shift in eV;* S_0^2 *is the amplitude reduction factor and was set to 0.9 for all standards. The CN uncertainty value includes an additional 15% added in quadrature to the CN uncertainty value calculated by the fitting algorithm to account for fixing* S_0^2 *to 0.9 (Calvin, 2013). *Indicates on RS birn sample one correlation higher than 0.95 between CN and* σ^2 *for the best fit (adding multiple scattering paths did not statistically improve the fit but did decrease this correlation). A Hanning window was used for both the forward (dk=1) and back (dr =0.5) Fourier transformation. All spectra were fit with a k weighting of 3. Spectra were fit simultaneously with k weights of 1, 2, and 3.*

Sample & CIF reference	R-factor & # in Table S3	N_{idp} & k-range fit	N_{var} & R-range fit	χ^2 & χ^2_n	Path	CN	R (Å)	σ^2 (Å^2)	ΔE (eV)	±CN	±R (Å)	±σ^2(Å^2) x10^{-3}	±ΔE (eV)
Ni-Acid birn.	0.007	13.5	9	3674	Ni-O	6.4	2.055	0.006	0.9	1.1	0.010	2	1.0
(Post and Veblen, 1990)	8	2.5 - 11.5	1.2 - 3.6	823	Ni-Mn	1.2	2.886	0.008	0.9	0.5	0.030	3	1.0
					Ni-Mn	5.5	3.494	0.008	0.9	1.7	0.014	3	1.0
RS birn.	0.007*	12.9	8	4704	Ni-O	7.6	2.053	0.007	5.0	1.3	0.009	1	0.9
(Post and Veblen, 1990)	9	2.5 - 12	1.2 - 3.4	956	Ni-Mn	3.0	3.468	0.007	5.0	2.5	0.017	7	0.9
					Ni-Mn	1.0	3.048	0.007	5.0	0.8	0.055	7	0.9
Ni-Kaolinite, pH 6	0.0115	10.3	6	598	Ni-O	6.1	2.069	0.005	2.8	1.1	0.011	2	1.0
(Saalfeld and Wedde, 1974)	11	2.5 - 10.3	1.1 - 3.2	139	Ni-Al	0.8	2.976	0.005	2.8	0.6	0.054	2	1.0
Ni kaolinite pH 7.5	0.0065	15.8	9	6343	Ni-O	6.0	2.038	0.006	-1.2	1.0	0.009	1	1.0
	12	2.5 - 13.5	1.1 - 3.4	929	Ni-Ni	4.7	3.028	0.009	-1.2	1.8	0.009	2	1.0
(Mellini and Viti, 1994)					Ni-Al	1.6	3.028	0.003	-1.2	1.1	0.009	3	1.0
					Ni-Si	1.9	3.238	0.003	-1.2	1.1	0.009	3	1.0
Ni-Fe LDH	0.0187	13.5	7	27998	Ni-O	6.0	2.076	0.006	2.0	1.1	0.011	2	0.9
(Mellini and Viti, 1994)	18	2.5 - 12.3	1 - 3.2	4293	Ni-Ni/Fe	7.0	3.104	0.008	2.0	1.9	0.010	2	0.9
Ni-Mg Oxalate 5%	0.0019	11.2	6	8083	Ni-O	7.5	2.048	0.006	1.7	1.2	0.004	1	0.5
(Soleimannejad et al., 2007)	24	2.5 - 13	1 - 2.7	1546	Ni-C	5.4	2.770	0.006	1.7	1.0	0.011	1	0.5
Ni-Citrate (s)	0.0029	11.4	6	16294	Ni-O	7.4	2.058	0.008	3.2	1.2	0.006	1	0.5
(Soleimannejad et al., 2007)	25	2.5 - 13.2	1.1 - 2.8	2995	Ni-C	2.3	2.897	0.008	3.2	0.7	0.032	1	0.5
Ni-Humic Acid	0.0013	11.4	6	1298	Ni-O	7.9	2.061	0.009	3.3	1.2	0.003	1	0.3
(Soleimannejad et al., 2007)	26	2.5 - 13.2	1 - 2.7	238	Ni-C	2.6	2.915	0.009	3.3	0.6	0.020	1	0.3
Serp96	0.021	8.9	6	1183	Ni-O	5.3	2.063	0.004	0.6	1.2	0.018	3	1.9
(Mellini and Viti, 1994)	28	2.5 - 10	1.1 - 3	411	Ni-Mg	1.6	3.074	0.004	0.6	1.1	0.049	3	1.9
Serp185	0.0134	10.3	7	1338	Ni-O	5.4	2.086	0.005	2.8	1.1	0.015	2	1.6
(Mellini and Viti, 1994)	29	2.5 - 10.4	1.2 - 3.3	409	Ni-Mg	4.2	3.059	0.016	2.8	3.6	0.039	15	1.6

Serp5811	0.0179	9.4	7	508	Ni-O	7.2	2.077	0.008	1.3	1.7	0.022	3	2.2
(Mellini and Viti, 1994)	30	2.5 - 10.4	1.2 - 3.1	216	Ni-Mg	4.0	3.058	0.008	1.3	3.0	0.036	10	2.2
JR3br	0.006	12.6	7	2591	Ni-O	6.3	2.060	0.006	-0.5	1.0	0.008	1	0.8
(Mellini and Viti, 1994)	31	2.5 - 12.2	1.2 - 3.3	460	Ni-Ni	1.2	3.113	0.004	-0.5	0.7	0.015	4	0.8
Ni-Goethite	0.024	12.7	8	4972	Ni-O	6.2	2.060	0.005	1.8	1.4	0.017	3	1.5
(Gualtieri and Venturelli, 1999)	38	2.5 - 10	1.2 - 3.9	1067	Ni-Fe/Ni	2.3	2.960	0.006	1.8	1.3	0.066	8	1.5
					Ni-Fe/Ni	2.3	3.137	0.006	1.8	1.3	0.061	8	1.5
Ni-Ferrihydrite	0.019	12.2	7	1925	Ni-O	8.1	2.055	0.008	-1.6	1.5	0.013	2	1.3
	39	2.5 - 11	1.1 - 3.4	369	Ni-Fe/Ni	6.7	3.027	0.023	-1.6	3.1	0.029	5	1.3
(Jansen et al., 2002)					Ni-Fe/Ni	6.7	3.641	0.023	-1.6	3.1	0.073	5	1.3
					Ni-Fe/Ni	6.7	3.447	0.023	-1.6	3.1	0.029	5	1.3
Ni-Hematite	0.022	23.3	12	3308	Ni-O	5.6	2.052	0.005	2.5	1.0	0.010	1	0.8
(Finger and Hazen, 1980)	40	2.5 - 12	1.2 - 5.1	294	Ni-Fe	10.4	2.951	0.017	2.5	3.2	0.013	4	0.8
					Ni-Fe	1.5	3.712	0.001	2.5	1.1	0.018	4	0.8
					Ni-O-Fe	3.1	3.890	0.007	2.5	2.2	0.018	2	0.8
					Ni-Fe	2.3	5.052	0.001	2.5	1.8	0.027	4	0.8
Ni-Magnetite	0.005	14.2	8	626	Ni-O	6.2	2.056	0.005	1.5	1.0	0.007	1	0.6
(O'Neill and Dollase, 1994)	41	2.5 - 12	1.2 - 3.6	100	Ni-Fe/Ni	7.7	2.974	0.008	1.5	1.6	0.008	1	0.6
					Ni-Fe/Ni	7.7	3.482	0.008	1.5	1.6	0.008	1	0.6
					Ni-O	6.2	3.570	0.008	1.5	1.0	0.035	1	0.6
Ni Foil	0.014	24.5	11	42755	Ni-Ni	10.9	2.480	0.006	-2.8	1.9	0.005	1	0.8
(Suh et al., 1988)	42	2.5 - 12.5	1.6 - 5.5	3170	Ni-Ni	7.1	3.486	0.010	-2.8	2.4	0.017	2	0.8
					Ni-Ni	29.0	4.334	0.010	-2.8	7.8	0.011	2	0.8
					Ni-Ni-Ni-Ni	24.1	5.045	0.010	-2.8	6.9	0.011	2	0.8
Awaruite	0.015	21.4	7	8044	Ni-Ni/Fe	7.8	2.499	0.007	-3.6	1.4	0.005	1	0.8
(Suh et al., 1988)	43	2.5 - 12	1.6 - 5.2	558	Ni-Ni/Fe	3.9	3.532	0.011	-3.6	0.7	0.005	1	0.8
					Ni-Ni/Fe	15.7	4.374	0.011	-3.6	2.7	0.012	1	0.8
					Ni-Ni-Ni-Ni	15.7	5.095	0.011	-3.6	2.7	0.012	1	0.8
s20unt silt	0.0041	14.1	8	1230	Ni-O	6.4	2.055	0.006	0.48	1.0	0.007	1	0.7
		2.5 - 12.3	1 - 3.3	201	Ni-Ni	1.8	3.060	0.005	0.48	0.5	0.020	2	0.7
(Carlson et al., 1988)					Ni-Mg	1.8	3.140	0.005	0.48	0.5	0.020	2	0.7
					Ni-Si	2.9	3.294	0.005	0.48	0.9	0.020	2	0.7

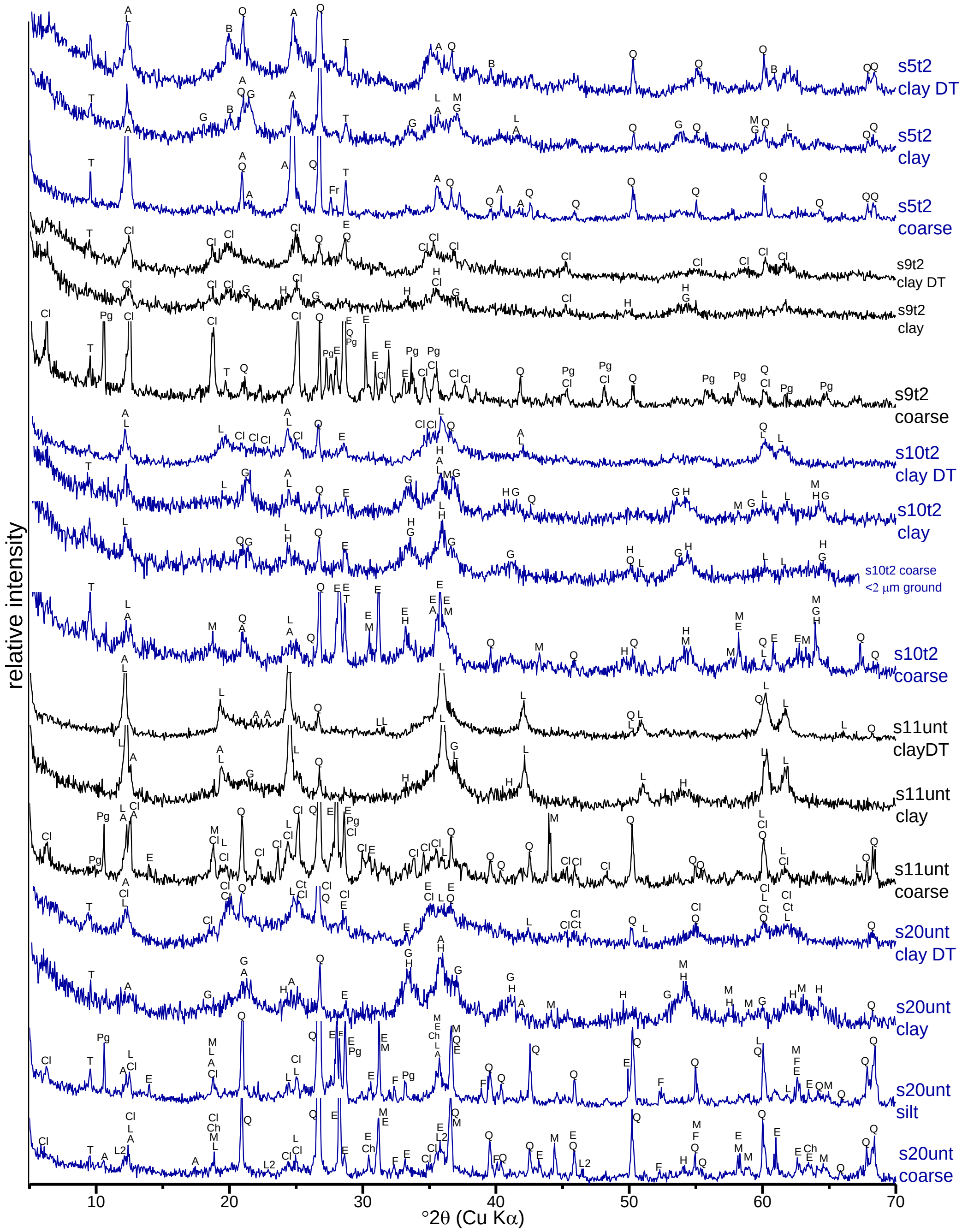

Figure S1. *XRD diffractograms of serpentine soils and soil fractions (sand, silt and clay fractions). "DT" indicates "Dithionite Treated" clay fractions that were treated with the citrate dithionite method to remove iron oxides. In the DT samples, the disappearance of peaks associated with hematite, magnetite and goethite can be noted when compared to the non-treated clay fractions. Quartz and clinochlore are also common. The clay fraction is commonly composed of serpentine minerals, iron oxides and clinochlore. MINERAL KEY: A – antigorite, B – brucite, Ch – chromite, Cl – clinochlore, Ct – chlorite, E – enstatite, F – forsterite, Fr – ferrosilite, G – goethite, H – hematite, L – lizardite, L2 - Lizardite 2H1, M – magnetite, Pg – pargasite, Q – quartz, T – talc.*

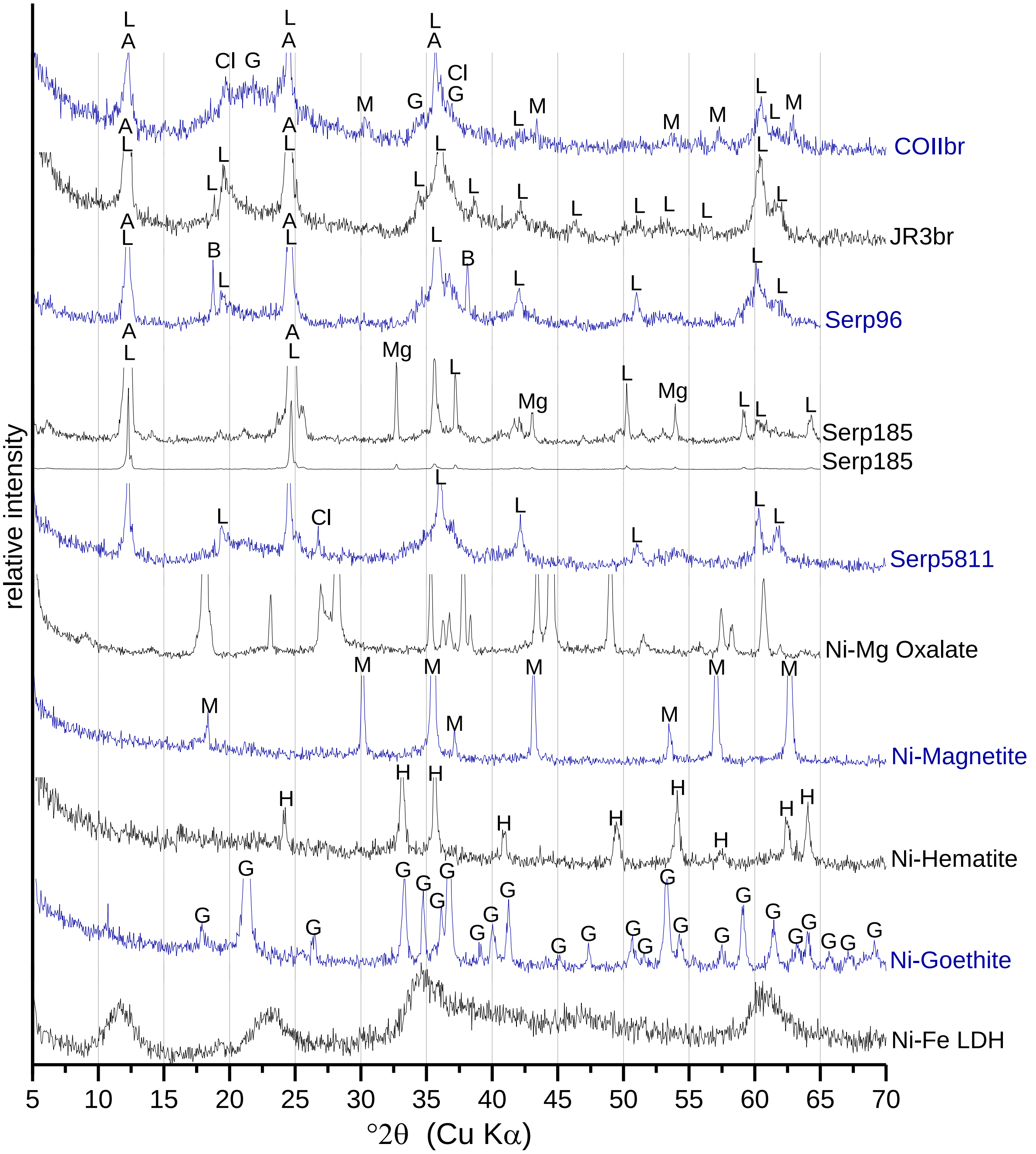

Figure S2. *XRD diffractograms of nickel enriched and serpentine minerals used as standards for EXAFS-LCF. A comparison of JR3 bedrock and serpentine mineral #96 indicates the bedrock is serpentine mineral. MINERAL KEY: A – antigorite, B – brucite, Cl – clinochlore, G – goethite, H – hematite, L – lizardite, M – magnetite, Mg – magnesite.*

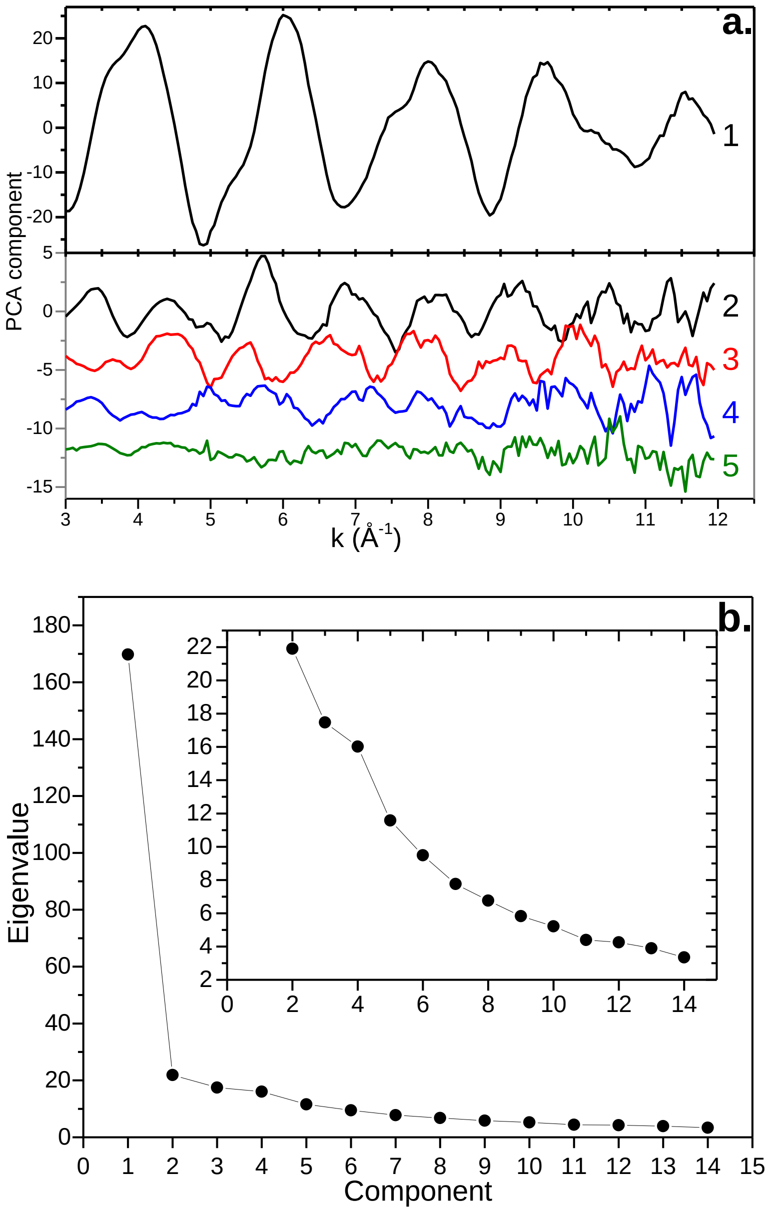

Figure S3. *Principal Component Analysis (PCA) results. The first five principal components, 1-5, indicate that at most four components could be used to reconstruct the data because after the fourth component, the noise contribution is larger than any discernable EXAFS oscillations. However, information from the scree plot* ***b.)*** *does not agree with this. The scree plot shows that the largest break in slope occurs at two components. There is another slight break in the slope at 4 components on the scree plot.*

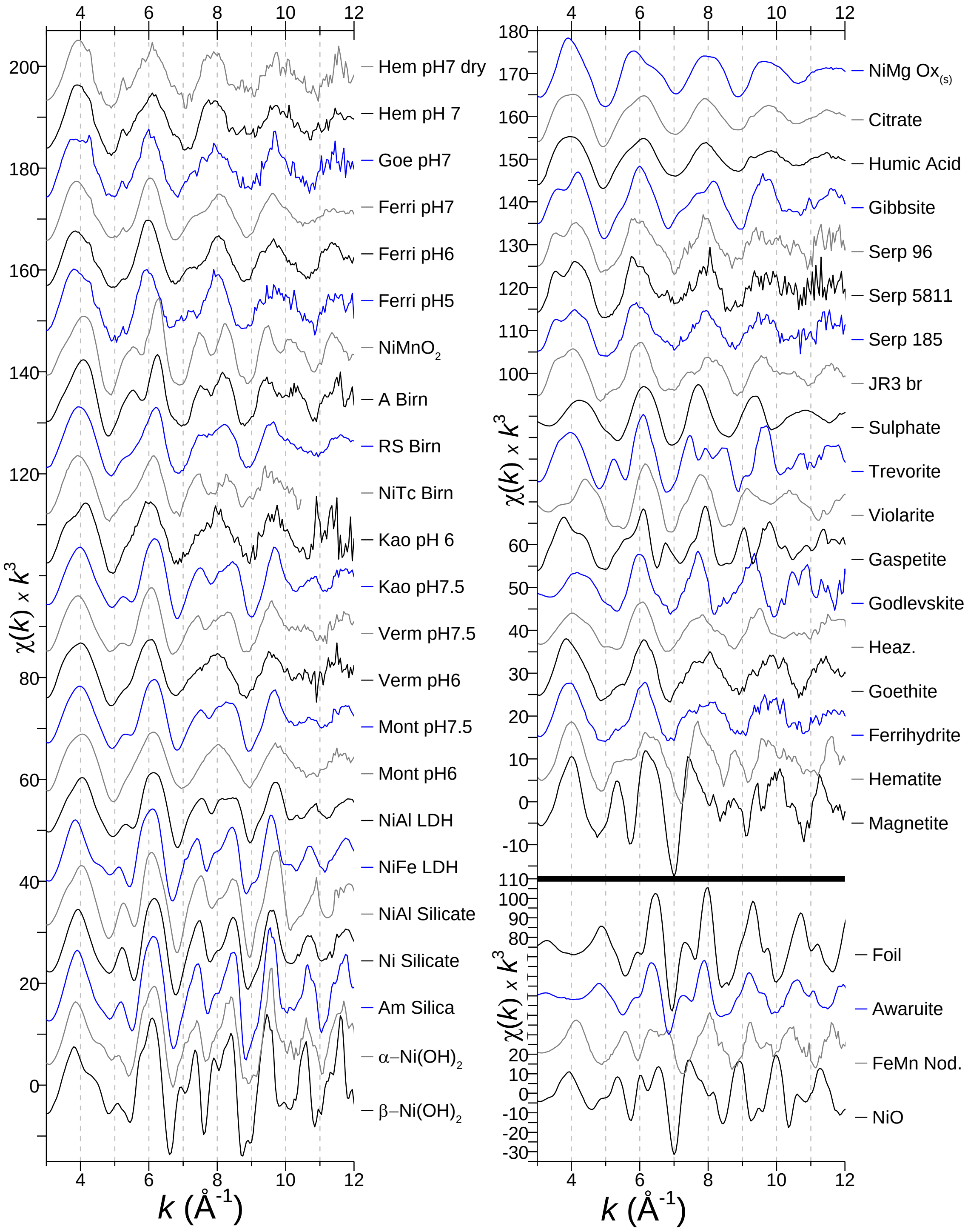

Figure S4. *EXAFS standards considered for LCF of serpentine soils and soil fractions. Sources and descriptions of each standard are indicated in Table S3.*

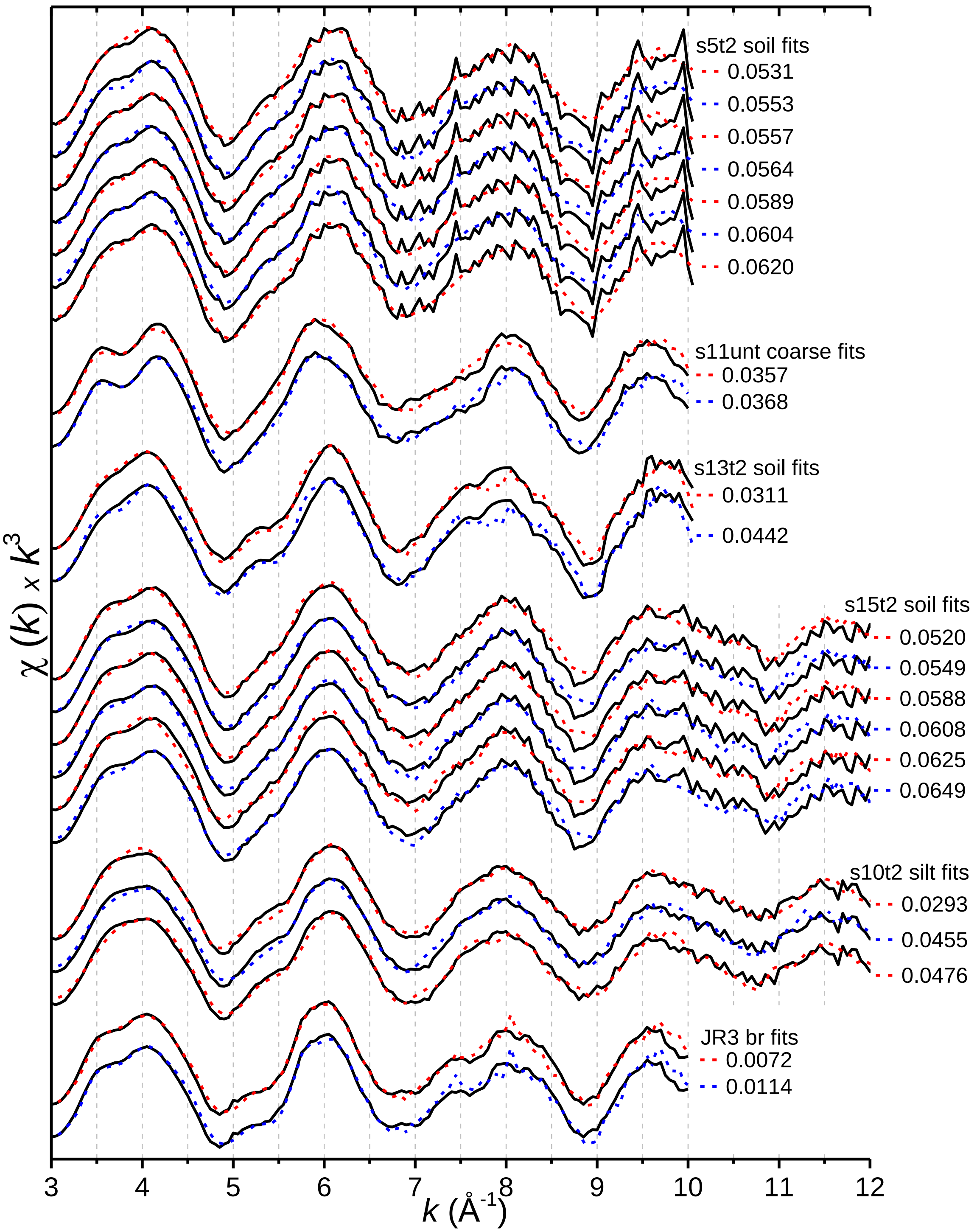

Figure S5. *LCF results of selected soils and JR3br. Data show how fitting statistics are very similar and choosing correct standards can be done sometimes by visual inspection of the fit. The differences in spectral fits at low k can be useful to eliminate standards and improve overall confidence in fits because the indentation in the first oscillation results from multiple scattering in long-range order of light elements (e.g., aluminum and magnesium).*

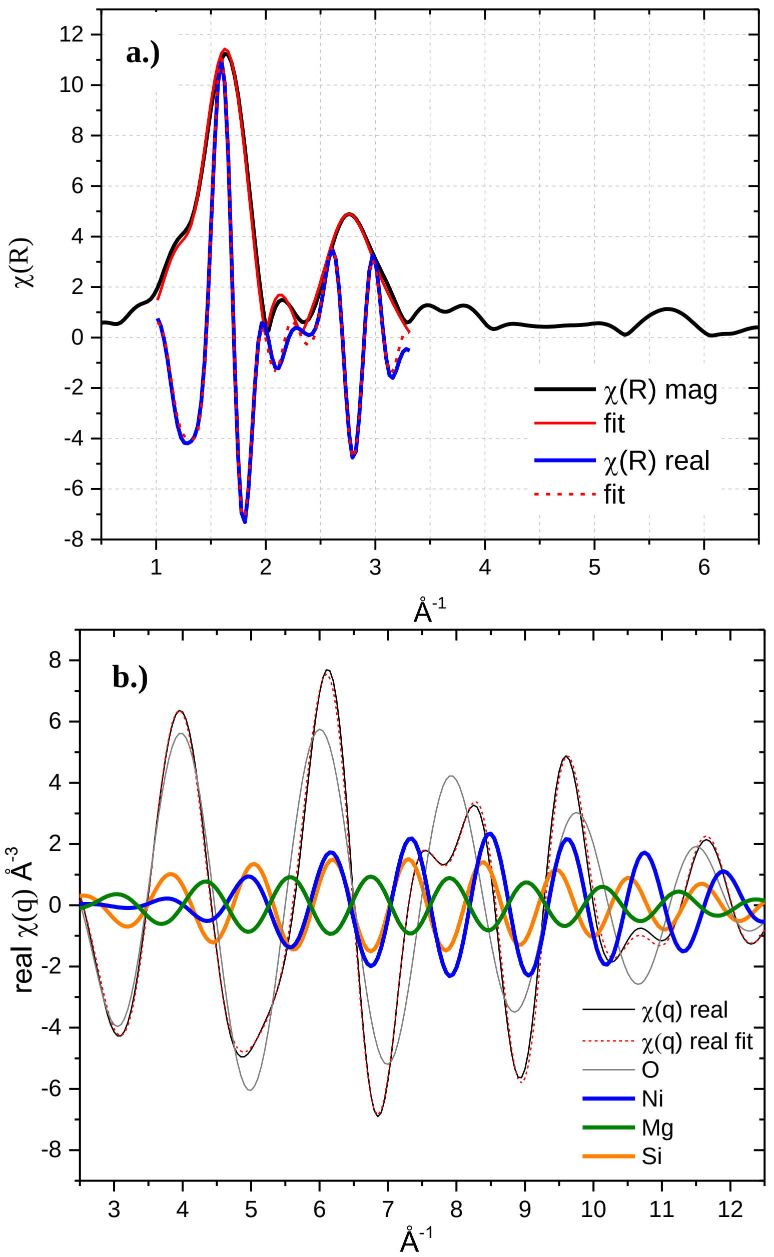

Figure S6. *EXAFS shell fitting of s20unt silt fraction. These data were fit using the crystal structure of enstatite. Results from the fit are at the end of Table S5.* ***Figure S6a*** *illustrates the magnitude and real part of the Fourier transformed EXAFS data.* ***Figure s6b*** *contains real part of the back-Fourier transformed data along with its fit. Additionally, the four scattering paths used in the fit [oxygen, gray; nickel, blue; magnesium, green; silicon, orange] are shown. Nickel, magnesium and silicon are the elements in the second shell. The nickel and magnesium (blue and green) are out of phase, which results in destructive interference and a decrease in the second shell amplitude. The silicon photoelectric scattering wave (orange), however, is in-phase with nickel throughout most of the k-range until about 10 Å^{-1}. The in-phase Si and Ni waves are additive, which increases the amplitude in the second shell. This constructive and destructive interference in the second shell is well documented for layered double hydroxides and phyllosilicates (see Main Text); however, it is not discussed for inosilicate minerals such as enstatite, which are common in mafic rocks. Particular emphasis is presented here to highlight that EXAFS spectra of inosilicate minerals can have similar features of a layered double hydroxide.*

REFERENCES

Arai, Y. (2008) Spectroscopic evidence for Ni(II) surface speciation at the iron oxyhydroxides - Water interface. *Environmental Science & Technology* 42, 1151-1156.

Calvin, S. (2013) *XAFS for Everyone*. CRC Press.

Carlson, W.D., Swinnea, J.S., Miser, D.E. (1988) Stability of orthoenstatite at high temperature and low pressure. *American Mineralogist* 73, 1255-1263.

Carvalho-E-Silva, M.L., Ramos, A.Y., Tolentino, H.C.N., Enzweiler, J., Netto, S.M., Alves, M. (2003) Incorporation of Ni into natural goethite: An investigation by X-ray absorption spectroscopy. *American Mineralogist* 88, 876-882.

Centofanti, T., Siebecker, M.G., Chaney, R.L., Davis, A.P., Sparks, D.L. (2012) Hyperaccumulation of nickel by *Alyssum corsicum* is related to solubility of Ni mineral species. *Plant Soil* 359, 71-83.

Downward, L., Booth, C.H., Lukens, W.W., Bridges, F. (2007) A variation of the F-Test for determining statistical relevance of particular parameters in EXAFS fits, in: Hedman, B., Painetta, P. (Eds.), *X-Ray Absorption Fine Structure-XAFS13*, pp. 129-131.

Drits, V.A., Lanson, B., Gaillot, A.-C. (2007) Birnessite polytype systematics and identification by powder X-ray diffraction. *American Mineralogist* 92, 771-788.

Fan, R., Gerson, A.R. (2011) Nickel geochemistry of a Philippine laterite examined by bulk and microprobe synchrotron analyses. *Geochim. Cosmochim. Acta* 75, 6400-6415.

Finger, L.W., Hazen, R.M. (1980) Crystal-structure and isothermal compression of Fe2O3,Cr2O3, and V2O3 to 50 kbars. *J. Appl. Phys.* 51, 5362-5367.

Ford, R.G., Scheinost, A.C., Scheckel, K.G., Sparks, D.L. (1999) The link between clay mineral weathering and the stabilization of Ni surface precipitates. *Environmental Science & Technology* 33, 3140-3144.

Gualtieri, A.F., Venturelli, P. (1999) In situ study of the goethite-hematite phase transformation by real time synchrotron powder diffraction. *American Mineralogist* 84, 895-904.

Hamilton, W.C. (1965) Significance tests on the crystallographic R factor. *Acta Crystallographica* 18, 502-510.

Herdtweck, E., Kornprobst, T., Sieber, R., Straver, L., Plank, J. (2011) Crystal structure, synthesis, and properties of tri-calcium di-citrate tetra-hydrate [Ca3(C6H5O7)2(H2O)2]·2H2O. *Zeitschrift für anorganische und allgemeine Chemie* 637, 655-659.

Jansen, E., Kyek, A., Schafer, W., Schwertmann, U. (2002) The structure of six-line ferrihydrite. *Appl. Phys. A-Mater. Sci. Process.* 74, S1004-S1006.

Kelly, S.D., Hesterberg, D., Ravel, B. (2008) Analysis of soils and minerals using X-ray absorption spectroscopy, in: Ulery, A.L., Drees, L.R. (Eds.), *Methods of Soil Analysis. Part 5. Mineralogical Methods*. Soil Science Society of America, Madison, WI

Lafferty, B.J., Ginder-Vogel, M., Zhu, M.Q., Livi, K.J.T., Sparks, D.L. (2010) Arsenite oxidation by a poorly crystalline manganese-oxide. 2. Results from X-ray absorption spectroscopy and X-ray diffraction. *Environmental Science & Technology* 44, 8467-8472.

Lakshmi Reddy, S., Ravindra Reddy, T., Siva Reddy, G., Endo, T., Frost, R.L. (2014) Synthesis and spectroscopic characterization of magnesium oxalate nano-crystals. *Spectrochimica Acta Part A: Molecular and Biomolecular Spectroscopy* 123, 25-29.

Malinowski, E.R. (1977) Determination of number of factors and experimental error in a data matrix. *Anal. Chem.* 49, 612-617.

Malinowski, E.R. (1978) Theory of error for target factor-analysis with applications to mass-spectrometry and nuclear magnetic-resonance spectrometry. *Analytica Chimica Acta-Computer Techniques and Optimization* 2, 339-354.

Manceau, A., Lanson, B., Drits, V.A. (2002) Structure of heavy metal sorbed birnessite. Part III: Results from powder and polarized extended X-ray absorption fine structure spectroscopy. *Geochim. Cosmochim. Acta* 66, 2639-2663.

Manceau, A., Lanson, M., Geoffroy, N. (2007) Natural speciation of Ni, Zn, Ba, and As in ferromanganese coatings on quartz using X-ray fluorescence, absorption, and diffraction. *Geochim. Cosmochim. Acta* 71, 95-128.

McNear, D.H., Chaney, R.L., Sparks, D.L. (2007) The effects of soil type and chemical treatment on nickel speciation in refinery enriched soils: A multi-technique investigation. *Geochim. Cosmochim. Acta* 71, 2190-2208.

Mellini, M., Viti, C. (1994) Crystal-structure of lizardite-1t from Elba, Italy. *American Mineralogist* 79, 1194-1198.

Mohandes, F., Davar, F., Salavati-Niasari, M. (2010) Magnesium oxide nanocrystals via thermal decomposition of magnesium oxalate. *Journal of Physics and Chemistry of Solids* 71, 1623-1628.

O'Neill, H.S.C., Dollase, W.A. (1994) Crystal structures and cation distributions in simple spinels from powder XRD structural refinements: MgCr2O4, ZnCr2O4, Fe3O4 and the temperature dependence of the cation distribution in ZnAl2O4. *Physics and Chemistry of Minerals* 20, 541-555.

Packter, A., Omomo, A. (1984) The coprecipitation of magnesium nickel oxalate dihydrate powders (solid solutions) from aqueous solution: Precipitate compositions and coprecipitate mechanisms. *Crystal Research and Technology* 19, 467-476.

Peacock, C.L., Sherman, D.M. (2007a) Crystal-chemistry of Ni in marine ferromanganese crusts and nodules. *American Mineralogist* 92, 1087-1092.

Peacock, C.L., Sherman, D.M. (2007b) Sorption of Ni by birnessite: Equilibrium controls on Ni in seawater. *Chem. Geol.* 238, 94-106.

Peltier, E., Allada, R., Navrotsky, A., Sparks, D.L. (2006) Nickel solubility and precipitation in soils: a thermodynamic study. *Clays and Clay Minerals* 54, 153-164.

Peltier, E., Lelie, D.v.d., Sparks, D.L. (2010) Formation and stability of Ni−Al hydroxide phases in soils. *Environmental Science & Technology* 44, 302-308.

Post, J.E., Veblen, D.R. (1990) Crystal structure determinations of synthetic sodium, magnesium, and potassium birnessite using TEM and the Rietveld method. *American Mineralogist* 75, 477-489.

Ravel, B., Newville, M. (2005) ATHENA, ARTEMIS, HEPHAESTUS: data analysis for x-ray absorption spectroscopy using Ifeffit. *Journal of Synchrotron Radiation* 12, 537-541.

Saalfeld, H., Wedde, M. (1974) *Refinement of the crystal structure of gibbsite, Al(OH)3, Zeitschrift für Kristallographie*, p. 129.

Saiah, F.B.D., Su, B.L., Bettahar, N. (2009) Nickel-iron layered double hydroxide (LDH): Textural properties upon hydrothermal treatments and application on dye sorption. *J. Hazard. Mater.* 165, 206-217.

Scheinost, A.C., Sparks, D.L. (2000) Formation of layered single- and double-metal hydroxide precipitates at the mineral/water interface: a multiple-scattering XAFS analysis. *J. Colloid Interface Sci.* 223, 167-178.

Schwertmann, U., Cornell, R.M. (1991) *Iron Oxides in the Laboratory*. VCH, Weinheim.

Singh, B., Sherman, D.M., Gilkes, R.J., Wells, M., Mosselmans, J.F.W. (2000) Structural chemistry of Fe, Mn, and Ni in synthetic hematites as determined by extended X-ray absorption fine structure spectroscopy. *Clays and Clay Minerals* 48, 521-527.

Singh, B., Sherman, D.M., Gilkes, R.J., Wells, M.A., Mosselmans, J.F.W. (2002) Incorporation of Cr, Mn and Ni into goethite (alpha-FeOOH): mechanism from extended X-ray absorption fine structure spectroscopy. *Clay Minerals* 37, 639-649.

Soleimannejad, J., Aghabozorg, H., Hooshmand, S., Ghadermazi, M., Gharamaleki, J.A. (2007) The monoclinic polymorph of catena-poly diaquamanganese(II) -mu-oxalato-kappa O-4(1),O-2:O-1 ',O-2 '. *Acta Crystallogr. Sect. E.-Struct Rep. Online* 63, M2389-U1294.

Soper, D. (2015) *Regularized Lower Incomplete Beta Function Calculator, Retrieved May 8, 2015, from http://www.danielsoper.com/statcalc3/calc.aspx?id=37*.

Suh, I.-K., Ohta, H., Waseda, Y. (1988) High-temperature thermal expansion of six metallic elements measured by dilatation method and X-ray diffraction. *Journal of Materials Science* 23, 757-760.

Wasserman, S.R., Allen, P.G., Shuh, D.K., Bucher, J.J., Edelstein, N.M. (1999) EXAFS and principal component analysis: a new shell game. *Journal of Synchrotron Radiation* 6, 284-286.

Webb, S.M. (2005) SIXpack: a graphical user interface for XAS analysis using IFEFFIT. *Phys. Scr.* T115, 1011-1014.

Wilson, M.J., Jones, D., McHardy, W.J. (1981) The weathering of serpentinite by Lecanora atra. *Lichenologist* 13, 167-176.

Wilson, M.J., Jones, D., Russell, J.D. (1980) Glushinskite, a naturally-occurring magnesium oxalate. *Mineralogical Magazine* 43, 837-840.

Yamaguchi, N.U., Scheinost, A.C., Sparks, D.L. (2002) Influence of gibbsite surface area and citrate on Ni sorption mechanisms at pH 7.5. *Clays and Clay Minerals* 50, 784-790.

Zhu, M.Q., Ginder-Vogel, M., Sparks, D.L. (2010) Ni(II) sorption on biogenic Mn-oxides with varying Mn octahedral layer structure. *Environmental Science & Technology* 44, 4472-4478.